A micromechanically inspired model for compressive and shear failure in fibre-reinforced composites

Downloaded from: https://research.chalmers.se, 2026-11-17 04:47 UTC

Citation for the original published paper (version of record):
Hertelendy, K., Gutkin, R., Larsson, R. (2026). A micromechanically inspired model for compressive and shear failure in fibre-reinforced
composites. Mechanics of Materials, 221(October 2026).
http://dx.doi.org/10.1016/j.mechmat.2026.105802

N.B. When citing this work, cite the original published paper.

research.chalmers.se offers the possibility of retrieving research publications produced at Chalmers University of Technology. It covers all kind of research output: articles, dissertations, conference papers, reports etc. since 2004. research.chalmers.se is administrated and maintained by Chalmers Library

(article starts on next page)

Mechanics of Materials 221 (2026) 105802

Contents lists available at ScienceDirect

Mechanics of Materials

journal homepage: www.elsevier.com/locate/mecmat

Research paper

A micromechanically inspired model for compressive and shear failure in fibre-reinforced composites

Krisztián Gy. Hertelendy [a,*], Renaud Gutkin [a,b], Ragnar Larsson [a]

[a] Department of Mechanical Engineering, Chalmers University of Technology, SE-412 96 Göteborg, Sweden
[b] Volvo Car Corporation, SE-405 31 Göteborg, Sweden

ARTICLE INFO

Invited Editor Ghatu Subhash

Keywords:
CFRP composites
Continuum damage mechanics
Homogenisation
Misaligned fibres
Fibre kinking

ABSTRACT

This paper introduces a 3D continuum damage mechanics (CDM) model formulated with nonlinear kinematics to describe the mechanical response of CFRP composites, focusing on their behaviour under compression and shear. The CFRP is modelled using matrix and fibre phases, where a computationally efficient mean-field averaging approach is used to obtain the homogenised composite response at the ply level. The two phases are modelled as hyperelastic materials, and continuum damage induced by shear degrades the matrix. To obtain a well-posed homogenisation in terms of a fluctuating displacement field in the Hill–Mandel condition, the model incorporates a rotation-neutralised formulation alongside matrix–fibre coupling formulated in terms of the consequent Biot stress. The performance of the model was assessed using measurements from the Third World-Wide Failure Exercise and experimental laminate tests. Using material parameters calibrated on the compressive curves for the IM7/8552 plies, the model results in biaxial failure envelopes with good qualitative and quantitative agreement with the LaRC05 and Hashin criteria. The computational model was also used to predict the compressive strength of multidirectional T700/epoxy laminates. On average, the strength predictions differed from the experimental mean by 6.1%, while the measurements showed an average difference from the mean of 3.8% based on three measurements for each lay-up. The model also compares favourably with two other representative models in the literature.

1. Introduction

Currently, there is no universally accepted standard approach for modelling damage and fracture in fibre-reinforced polymers (FRP). Many competing analytical expressions for failure envelopes and constitutive models can be found in the literature, as demonstrated in the World-Wide Failure Exercises (WWFE Hinton, 2004, WWFE-II Hinton and Kaddour, 2012, WWFE-III Kaddour et al., 2013a). The difficulties in predicting failure in FRPs arise from the different failure modes that can develop on different length scales simultaneously and even interact with each other. Furthermore, failure is greatly influenced by many factors related to material quality, manufacturing, and reinforcement type. There is also generally a larger scatter in the experimental data compared to that in metals due to higher uncertainties in manufacturing and nonuniform microstructure.

Failure of composites in compression is of great interest in many different sectors, such as the automotive, aerospace, marine, and sports industries. In the current paper, intraply compressive failure and damage propagation are investigated in carbon-fibre reinforced polymers (CFRP) with a high fibre volume fraction; although the model may also be applied to different FRP composites, provided that the assumptions presented in later parts of the paper are fulfilled.

In recent decades, multiple comprehensive 3D models have been proposed for UD composites at the ply level. Pinho et al. released a two-part paper (Pinho et al., 2006a,b) on physically based failure models and their finite element implementation as a VUMAT user-defined subroutine in Abaqus. They used Mohr–Coulomb based criteria for matrix-dominated compressive failure modes to identify the initiation of crack formation. After failure initiation, the traction components on the (fixed) fracture surface, calculated from the continuum stress tensor via an orthotropic friction law, are degraded. In the finite element implementation, failure is smeared over the finite element in a dissipated energy-preserving manner to avoid mesh size dependency. The model provided good agreement with experimental failure envelopes for combined transverse normal — in-plane shear loading. Furthermore, the authors reproduced experimentally observed features of progressive damage propagation in standard test specimens tested in shear, longitudinal, and transverse compression.

* Corresponding author.
E-mail address: krisztian.hertelendy@chalmers.se (K.G. Hertelendy).

https://doi.org/10.1016/j.mechmat.2026.105802
Received 13 February 2026; Received in revised form 16 May 2026; Accepted 3 July 2026
Available online 9 July 2026
0167-6636/© 2026 The Authors. Published by Elsevier Ltd. This is an open access article under the CC BY license (http://creativecommons.org/licenses/by/4.0/).

The CompDam DGD code by NASA (Leone et al., 2019) is also implemented as a VUMAT subroutine for Abaqus. It is based on an additive decomposition of the deformation gradient tensor in an element according to Leone (2015). This formulation makes it possible to model high localised strains around cracks and fibre rotation during fibre-kinking failure, which affect a volume smaller than the finite element size. The second phase, in addition to the undamaged bulk material, involves the cracked material during compressive and shear matrix failure, as well as a kink-band region during fibre-kinking failure. Material softening results from a traction-based cohesive damage model during compressive and shear matrix failure, and from progressive fibre rotation in the kink-band region during fibre-kinking failure. The model shows good agreement with a micromechanical model for longitudinal compression (Bergan et al., 2020) and with experimental results for double-edge notch compression specimens (Bergan and Jackson, 2018).

To resolve matrix–fibre interactions at the ply level, an efficient multiscale homogenisation method is required. While FE-based variational homogenisation frameworks exist, including the Hill–Mandel condition, cf. Larsson et al. (2010), their computational cost is often prohibitive. Classical micromechanics models, such as self-consistent schemes based on Eshelby's inclusion theory (Eshelby, 1957), face limitations for strongly non-linear long-fibre composites. In this context, we also note that the finite-volume direct averaging method (Khatam and Pindera, 2009) offers a computationally efficient alternative without FE discretisation.

Singh et al. (2024) used a computational homogenisation scheme based on the Hill–Mandel condition to obtain the effective composite response from that of the constituents. To circumvent the computational burden of fully resolved microscale simulations, a mean-field homogenisation was developed, combined with isostatic stress assumptions transverse to fibres. The authors applied a viscoelastic/viscoplastic matrix model combined with continuum damage to model the rate-dependent quasi-brittle compressive response observed in experiments. Similar continuum damage models to the one proposed here were suggested by Larsson et al. (2018, 2023), where the ply response is based on elastic damage that uses rate-dependent damage evolution laws to achieve a mesh-objective response. The composite ply is treated as an anisotropic continuum in Larsson et al. (2018), simultaneously degrading parts of the free energy density function, and the rate of degradation of the different parts may be calibrated for various failure modes. Moreover, in order to handle the effect of fibre misalignment, a kinematically non-linear approach was used.

In the present paper, the homogenisation scheme by Singh et al. (2024) is further advanced in terms of isostatic stress conditions imposed transversely to the orientation of the fibre in the RVE. Moreover, to motivate the microscopic displacement field of the RVE as a Taylor expansion of the macro displacement, we formulate a rotation-neutralised formulation. This is crucial to obtaining a well-posed homogenisation problem when imposing the isostatic stress conditions.

Damage is only assumed in the matrix, and with a micromechanically inspired model for strain localisation in the matrix, the same damage law can be used for different matrix-driven failure modes. This reduces the number of modelling parameters and allows the same set of parameters to be used for the different failure modes presented in Section 2.

2. Failure modes

To motivate the choice of material models on the microscale, failure modes in uniaxial longitudinal and transverse compression, as well as in shear, are presented in this Section.

Under pure longitudinal compression, today's high-performance CFRP composites fail dominantly in fibre kinking, where failure is triggered by an initial fibre misalignment, leading to localised shear strain in the matrix. This, in turn, results in even larger rotation of the fibres locally, leading to a positive-feedback loop.

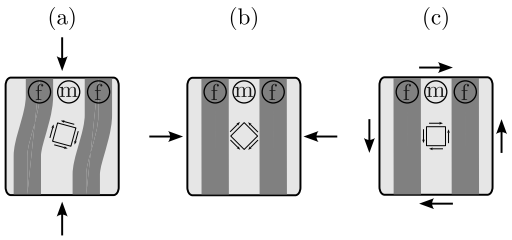

Fig. 1. Planes of maximum shear in the matrix in (a) longitudinal compression in the presence of initial imperfections, (b) transverse compression, and (c) in-plane shear. textcircledf — fibre, ⓜ — matrix.

One of the first works to attribute fibre-kinking failure as a geometrical imperfection-driven phenomenon was by Argon (1972), who assumed a local region of finite initial misalignment in the composite. By neglecting fibre rotation before collapse, he derived a simple expression for the longitudinal compressive strength of unidirectionally reinforced (UD) plies as a function of the shear strength and the initial misalignment angle.

Budiansky (1983) extended Argon's theory first by considering an elastic–perfectly plastic shear curve and derived the longitudinal compressive strength, which was also dependent on the shear yield limit. Later, Budiansky and Fleck (1993) derived an expression for longitudinal compressive strength, assuming strain-hardening plasticity in shear, expressed in a Ramberg–Osgood form. These works of Budiansky have later become known as fibre kinking theory (FKT).

We note that in UD composites with highly aligned fibres, it is possible to trigger fibre crushing before kinking failure in pure longitudinal compression, although it requires a small misalignment distribution in the ply, as well as a high level of alignment between the fibre and the load. This could not be found in most applications and is therefore not considered here.

According to Dávila and Camanho (2003), the fracture plane in pure transverse compression is oriented at $53°\pm2°$ to the loading direction for most technical composites. Failure is mainly driven by the shear stress in the matrix. The fact that the fracture plane is not oriented at 45° (as would be the case for pure shear failure) was explained in Dávila and Camanho (2003) by additional friction forces acting on microcracks that shift the fracture angle from the angle of maximum shear stress.

Shear cusps observed on fracture surfaces in shear tests (see, e.g., Melin et al. 2000) are indications of matrix shear dominated failure. Recently, Bai et al. (2025) carried out a DVC analysis on tensile tests of $[45°/-45°]_{2S}$ CFRP laminates at different temperatures. They found high shear strains before failure in the sample tested at room temperature, which then caused the specimen to fail via microcrack initiation in the matrix.

As shown in all of the above cases, the shear nonlinearity of the matrix not only contributes to the nonlinearity in the stress–strain curve before failure for transverse compression and shear cases but also plays a crucial role in fracture initiation. Fig. 1 shows the planes of maximum matrix shear stress in idealised uniaxial load cases and simple shear. During fibre kinking, matrix shear is highest in the frame attached to the misaligned fibres caused by their rotation. In the other two cases, the maximum matrix shear coincides with the frame of maximum composite shear.

3. Macroscale continuum damage mechanics model

A macroscale continuum damage mechanics (CDM) model is outlined below, which captures some of the main features of the deformation and failure process in a computationally efficient manner. Assuming that nonlinearity originates from both the matrix's nonlinearity and geometric nonlinearity due to fibre rotations, the model exploits the fact that failure in compression and shear is primarily caused by

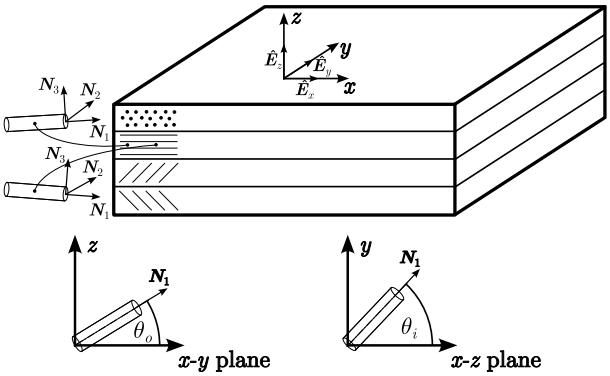

Fig. 2. Definition of the local and global coordinate systems and in-plane and out-of-plane fibre angles.

matrix shear failure. The maximum shear planes of the matrix that drive strain localisation and failure are different for the different compression/shear failure modes, as shown in Fig. 1. In addition, to avoid overly computationally demanding microscale simulations, a mean-field homogenisation approach with nonlinear kinematics is employed to account for the spatially varying material properties. The definition of the structure tensors used to define the transversely isotropic model is presented in Section 3.1. The kinematical assumptions on the microscale and the corresponding effective response are detailed in Section 3.2. Finally, the constitutive relations of the fibre and the matrix are concluded in Section 3.3.

3.1. Structure tensors of the fibres

Fibre orientation plays a significant role in the modelling of the mechanical response of UD plies. The local reinforcement orientation at a material point is denoted by the orientation vector $\boldsymbol{N}_1$ in the material configuration, as illustrated in Fig. 2. If transverse isotropy or isotropy of the fibres is assumed, the other two orthogonal unit vectors $\boldsymbol{N}_2$ and $\boldsymbol{N}_3$ can be freely chosen in the normal plane to form the basis $\{\boldsymbol{N}_1, \boldsymbol{N}_2, \boldsymbol{N}_3\}$ of a local 123 coordinate system attached to the fibres in the undeformed state.

We allow $\boldsymbol{N}_1$ to be arbitrarily orientated, representing the combination of ply orientation and initial local fibre misalignment. The orientation vector $\boldsymbol{N}_2$ is then chosen as an in-plane component of the ply with respect to the laminate coordinate system and $\boldsymbol{N}_3 = \boldsymbol{N}_1 \times \boldsymbol{N}_2$.

The global xyz coordinate system is defined by the unit vectors $\hat{\boldsymbol{E}}_x$, $\hat{\boldsymbol{E}}_y$, and $\hat{\boldsymbol{E}}_z$, where $\hat{\boldsymbol{E}}_z$ is aligned with the out-of-plane direction of a flat panel, and $\hat{\boldsymbol{E}}_x$ points in the nominal longitudinal direction of the laminate.

Although structural simulations often consider only the nominal fibre direction, out-of-plane initial misalignment plays a significant role in the initiation of out-of-plane fibre kinking. As shown in Fig. 2, if the fibres have an initial angle θ_i to the $x-z$ plane (representing in-plane rotation of the fibres from the reference x direction) and an angle θ_o to the x–y plane (representing out-of-plane rotation of the fibres from the reference x direction), then the vectors $\boldsymbol{N}_1$, $\boldsymbol{N}_2$, and $\boldsymbol{N}_3$ can be expressed in the coordinate system with the basis $\{\hat{\boldsymbol{E}}_x, \hat{\boldsymbol{E}}_y, \hat{\boldsymbol{E}}_z\}$ as

$$\boldsymbol{N}_1 = \kappa \hat{\boldsymbol{E}}_x + \sin[\theta_i]\hat{\boldsymbol{E}}_y + \sin[\theta_o]\hat{\boldsymbol{E}}_z, \tag{1a}$$

$$\boldsymbol{N}_2 = -\frac{\sin[\theta_i]}{\cos[\theta_o]}\hat{\boldsymbol{E}}_x + \frac{\kappa}{\cos[\theta_o]}\hat{\boldsymbol{E}}_y, \tag{1b}$$

$$\boldsymbol{N}_3 = -\kappa \tan[\theta_o]\hat{\boldsymbol{E}}_x - \sin[\theta_i]\tan[\theta_o]\hat{\boldsymbol{E}}_y + \cos[\theta_o]\hat{\boldsymbol{E}}_z \tag{1c}$$

where $\kappa = \sqrt{\cos^2[\theta_i] + \cos^2[\theta_o] - 1}$. Throughout this paper, square brackets $[\bullet]$ are used to denote a function of $\bullet$.

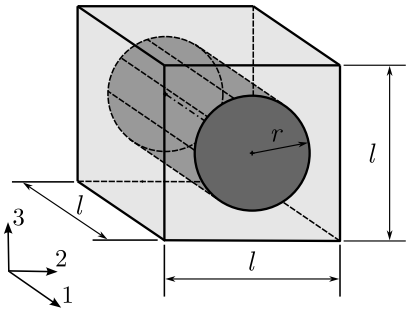

Fig. 3. A representative volume element (RVE) of the microstructure of an undeformed UD ply.

Furthermore, if only in-plane rotation is considered ($\theta_o = 0$), the expressions can be simplified to

$$\boldsymbol{N}_1 = \cos[\theta_i]\hat{\boldsymbol{E}}_x + \sin[\theta_i]\hat{\boldsymbol{E}}_y, \tag{2a}$$

$$\boldsymbol{N}_2 = -\sin[\theta_i]\hat{\boldsymbol{E}}_x + \cos[\theta_i]\hat{\boldsymbol{E}}_y, \tag{2b}$$

$$\boldsymbol{N}_3 = \hat{\boldsymbol{E}}_z. \tag{2c}$$

Using the set of local basis vectors, the following structure tensors are defined for the fibre response:

$$\boldsymbol{M}_{ij} = \frac{1}{2}\left(\boldsymbol{N}_i \otimes \boldsymbol{N}_j + \boldsymbol{N}_j \otimes \boldsymbol{N}_i\right),\ i,j \in \{1,2,3\},\ i \le j \tag{3}$$

3.2. Effective (homogenised) response

To define microscale kinematics, we introduce a representative volume element (RVE) of a unidirectionally reinforced composite ply, assuming uniform square packing, as shown in Fig. 3, where r is the fibre radius, l is the size of the RVE, and $v^f = r^2\pi/l^2$ is the fibre volume fraction. Strain fluctuations can be extensive in the matrix of a unit cell (RVE), especially in the vicinity of the fibre–matrix interfaces. In order to capture all consequences of strain and stress concentrations, a detailed micromechanical analysis may be needed, dramatically increasing the computational cost. To avoid this, an effective matrix model with strains smeared over the RVE is considered to simulate the homogenised response of the composite.

The following assumptions are considered on the microscale:

1. The deformation field is piecewise constant on the microscale and constant in one phase (matrix or fibre).
2. The longitudinal stretch in the fibres and matrix coincides.
3. The backrotated traction components in the fibres and matrix coincide in the longitudinal–transverse planes and are perpendicular to the fibres.
4. The macroscale rotation tensor of the composite accurately approximates the local rotation of the fibres and the matrix.

Assumption 1 is a simplification of the microscale fluctuations, similar to that of classical mean-field homogenisation schemes. Since there is no imposed boundary value problem on the RVE to be solved, specific assumptions are made to account for the interaction between the two phases. This also motivates the need for rotation neutralisation. These assumptions are summarised in Assumptions 2 and 3.

Assumption 2 holds until the fibres do not slip relative to the matrix. As long as there is strong matrix–fibre cohesion and the matrix cracks do not interfere with the fibre–matrix interface, it is a reasonable assumption. However, it is nevertheless a limitation of the model that needs to be addressed if fibre pull-out is expected during failure.

Assumption 3, i.e., traction continuity in the longitudinal–transverse planes and transverse to the fibres, is assumed as the simplest reasonable simplification of the high-complexity three-dimensional stress

distributions in these planes. We note that the assumption is made on the traction that is rotated back to the reference coordinate system (but not pulled back to the reference configuration) due to the formulation in terms of the nonsymmetric Biot stress tensor.

Assumption 4 refers to the assumption that the same rigid body rotation can be used in the polar decomposition in the fibres and the matrix phases, namely the rotation of the composite. The assumption is expected to hold under pure longitudinal and transverse compression. For highly localised shear strains in the matrix, the fibre rotation is expected to have a significant local fluctuation from the macro-rotation.

To derive the effective (homogenised) response of the matrix–fibre composite, consider again the representative 3D region, denoted by B_0, of the reference (undeformed) configuration for a UD ply, as shown in Fig. 3. The matrix material occupies the region B_0^m, and the fibre material occupies the region B_0^f. Consider also the microscale displacement gradient field in the RVE defined as $\boldsymbol{H} = \boldsymbol{u} \otimes \nabla_{\boldsymbol{X}}$ ($\boldsymbol{u}[\boldsymbol{X}]$ is the microscale displacement field) split into a macroscale constant displacement gradient $\bar{\boldsymbol{H}} = \bar{\boldsymbol{u}} \otimes \nabla_{\boldsymbol{X}}$ of the RVE (where $\bar{\boldsymbol{u}}$ is the macroscale displacement field) and a fluctuating portion $\tilde{\boldsymbol{H}} = \tilde{\boldsymbol{u}} \otimes \nabla_{\boldsymbol{X}}$. Here and in the following, the quantities with a bar above ($\bar{\bullet}$) refer to macroscale (composite) quantities, and the quantities with a tilde over ($\tilde{\bullet}$) refer to microscale fluctuations. The microscale quantities in the RVE are constructed as the sum of these two as $\bullet = \bar{\bullet} + \tilde{\bullet}$. From a Taylor series expansion of $\bar{\boldsymbol{u}}$ across the RVE, we find that the total microscale displacement gradient in B_0 is approximated linearly as

$$\boldsymbol{H} = \bar{\boldsymbol{H}} + \tilde{\boldsymbol{H}} \tag{4}$$

from which the microscale deformation gradient can be obtained as

$$\boldsymbol{F} = \boldsymbol{I} + \boldsymbol{H} = \boldsymbol{I} + \bar{\boldsymbol{H}} + \tilde{\boldsymbol{H}} = \bar{\boldsymbol{F}} + \tilde{\boldsymbol{H}} \tag{5}$$

where $\boldsymbol{I}$ is the second order identity tensor, $\bar{\boldsymbol{F}}$ the macroscale deformation gradient (constant in the RVE), and $\boldsymbol{F}$ the microscale deformation gradient.

To achieve a well-posed homogenisation-based model invariant to rigid-body rotations, we propose a rotation-neutralised formulation. To this end, by the right-polar decomposition of the macroscale deformation gradient, we have the relation

$$\bar{\boldsymbol{F}} = \bar{\boldsymbol{R}} \cdot \bar{\boldsymbol{U}} \tag{6}$$

where $\bar{\boldsymbol{R}}$ is the continuum rotation tensor, which, according to Assumption 4, is also the rotation in the fibres and matrix, i.e. $\boldsymbol{R} = \bar{\boldsymbol{R}}$. Furthermore, $\bar{\boldsymbol{U}}^2 = \bar{\boldsymbol{C}}$ where $\bar{\boldsymbol{C}}$ is the right Cauchy–Green symmetric deformation tensor. This leads to

$$\boldsymbol{F} = \bar{\boldsymbol{F}} + \tilde{\boldsymbol{H}} = \bar{\boldsymbol{R}} \cdot \bar{\boldsymbol{U}} + \tilde{\boldsymbol{H}} = \bar{\boldsymbol{R}} \cdot \boldsymbol{U} \tag{7}$$

where $\boldsymbol{U} = \bar{\boldsymbol{U}} + \tilde{\boldsymbol{H}}_R$. Moreover, $\tilde{\boldsymbol{H}}_R = \bar{\boldsymbol{R}}^\top \cdot \tilde{\boldsymbol{H}}$ is the rotation-neutralised material displacement gradient of the fluctuating displacement field that needs to be further specialised as discussed in the following. The associated virtual displacement gradient is

$$\begin{aligned} \delta\boldsymbol{F} &= \delta\boldsymbol{H} = \bar{\boldsymbol{R}} \cdot \delta\boldsymbol{U} + \delta\bar{\boldsymbol{R}} \cdot \boldsymbol{U} \\ &= \bar{\boldsymbol{R}} \cdot \left(\delta\bar{\boldsymbol{U}} + \delta\tilde{\boldsymbol{H}}_R\right) + \delta\bar{\boldsymbol{R}} \cdot \boldsymbol{U} \end{aligned} \tag{8}$$

with $\delta\tilde{\boldsymbol{H}}_R = \bar{\boldsymbol{R}}^\top \cdot \delta\tilde{\boldsymbol{H}}$.

Related to rotation-neutralised kinematics, we also obtain the corresponding stress response

$$\boldsymbol{P} = \boldsymbol{F} \cdot \boldsymbol{S} = \bar{\boldsymbol{R}} \cdot \boldsymbol{T}[\boldsymbol{U}] \text{ with } \boldsymbol{T} := \boldsymbol{U} \cdot \boldsymbol{S}, \tag{9}$$

where $\boldsymbol{S}$ is the second Piola Kirchhoff stress and $\boldsymbol{T}$ is the (generally nonsymmetric) Biot stress.

For the homogenised response, the Hill–Mandel (HM) energy equivalence condition for the homogenised response states that the microscale virtual work is the virtual work performed by the microscale stress response in the RVE in Fig. 3. First, we note that

$$\begin{aligned} \delta\boldsymbol{F} : \boldsymbol{P} &= \left(\boldsymbol{R} \cdot \left(\delta\boldsymbol{U} + \delta\tilde{\boldsymbol{H}}_R\right)\right) : (\boldsymbol{R} \cdot \boldsymbol{T}) + (\delta\boldsymbol{R} \cdot \boldsymbol{U}) : (\boldsymbol{R} \cdot \boldsymbol{T}) \\ &= \left(\underbrace{\boldsymbol{R}^\top \cdot \boldsymbol{R}}_{\boldsymbol{I}} \cdot \left(\delta\boldsymbol{U} + \delta\tilde{\boldsymbol{H}}_R\right)\right) : \boldsymbol{T} + \left(\boldsymbol{R}^\top \cdot \delta\boldsymbol{R}\right) : (\boldsymbol{T} \cdot \boldsymbol{U}) \\ &= \left(\delta\boldsymbol{U} + \delta\tilde{\boldsymbol{H}}_R\right) : \boldsymbol{T} + \underbrace{\left(\boldsymbol{R}^\top \cdot \delta\boldsymbol{R}\right) : (\boldsymbol{U} \cdot \boldsymbol{S} \cdot \boldsymbol{U})}_{\boldsymbol{O}} \\ &= \left(\delta\boldsymbol{U} + \delta\tilde{\boldsymbol{H}}_R\right) : \boldsymbol{T}, \end{aligned} \tag{10}$$

where $\boldsymbol{O}$ is the second-order zero tensor. We used the result that $\boldsymbol{R}^\top \cdot \delta\boldsymbol{R}$ is skew-symmetric and $\boldsymbol{U} \cdot \boldsymbol{S} \cdot \boldsymbol{U}$ is symmetric in the derivation. With a similar derivation, it can be seen that $\delta\bar{\boldsymbol{F}} : \bar{\boldsymbol{P}} = \delta\bar{\boldsymbol{U}} : \bar{\boldsymbol{T}}$. Hence, the virtual work equivalence

$$\delta\bar{\boldsymbol{F}} : \bar{\boldsymbol{P}} = \frac{1}{V_\square} \int_{B_0} \delta\boldsymbol{F} : \boldsymbol{P}\, dV \tag{11}$$

can be reformulated in terms of the right stretch tensor and the Biot stress as

$$\delta\bar{\boldsymbol{U}} : \bar{\boldsymbol{T}} = \frac{1}{V_\square} \int_{B_0} \delta\bar{\boldsymbol{U}} : \boldsymbol{T}\, dV + \frac{1}{V_\square} \int_{B_0} \delta\tilde{\boldsymbol{H}}_R : \boldsymbol{T}\, dV \tag{12}$$

where $V_\square$ is the volume of the RVE, that is, $V_\square = \int_{B_0} dV$.

Considering the matrix region B_0^m and the fibre region B_0^f, we assume a simple but representative homogenised response of the composite based on a piecewise constant deformation in B_0 so that

$$\tilde{\boldsymbol{H}}_R = \begin{cases} \tilde{\boldsymbol{H}}_R^m & \text{in } B_0^m \\ \tilde{\boldsymbol{H}}_R^f & \text{in } B_0^f \end{cases}, \quad \boldsymbol{T} = \begin{cases} \boldsymbol{T}^m & \text{in } B_0^m \\ \boldsymbol{T}^f & \text{in } B_0^f \end{cases} \tag{13}$$

Hence, Eq. (12) can be rewritten as

$$\delta\bar{\boldsymbol{U}} : \bar{\boldsymbol{T}} = \delta\bar{\boldsymbol{U}} : \left(v^m \boldsymbol{T}^m + v^f \boldsymbol{T}^f\right) + \frac{1}{V_\square} \int_{B_0} \delta\tilde{\boldsymbol{H}}_R : \boldsymbol{T}\, dV \tag{14}$$

where $v^f = V_\square^f / V_\square$ is the fibre volume fraction and $v^m = 1 - v^f$ the matrix volume fraction. Furthermore, the intrinsic stresses of the homogenised matrix and fibre $\boldsymbol{T}^m$, $\boldsymbol{T}^f$ are defined as

$$\boldsymbol{T}^m = \frac{1}{V_\square^m} \int_{B_0^m} \boldsymbol{T}\, dV\,, \quad \boldsymbol{T}^f = \frac{1}{V_\square^f} \int_{B_0^f} \boldsymbol{T}\, dV \tag{15}$$

where $V_\square^m$ is the volume of the matrix in B_0 and $V_\square^f$ is the volume of the fibre in the RVE.

In addition to the HM condition, the kinematic compatibility condition for the fluctuating $\boldsymbol{H}$ field reads

$$\frac{1}{V_\square} \int_{B_0} \tilde{\boldsymbol{H}}_R\, dV = \boldsymbol{O} \tag{16}$$

which gives

$$\tilde{\boldsymbol{H}}_R^f = -\frac{v^m}{v^f} \tilde{\boldsymbol{H}}_R^m \tag{17}$$

To adhere to Assumptions 2 and 3 regarding the deformation in the matrix/fibre microstructure, we choose $\tilde{\boldsymbol{H}}_R$ to be a symmetric strain tensor in terms of the structure tensors (3) defined as

$$\tilde{\boldsymbol{H}}_R = a_{22}\boldsymbol{M}_{22} + a_{33}\boldsymbol{M}_{33} + a_{12}\boldsymbol{M}_{12} + a_{13}\boldsymbol{M}_{13} = a_\alpha \boldsymbol{M}_\alpha \tag{18}$$

where α is summed over the indices $11, 22, 12, 13$ and a_{22}, a_{33}, a_{12}, and a_{13} are piecewise constant scalar fields so that

$$a_\alpha = \begin{cases} a_\alpha^m & \text{in } B_0^m \\ a_\alpha^f & \text{in } B_0^f \end{cases} \tag{19}$$

From Eq. (16) it follows that $v^m a_\alpha^m + v^f a_\alpha^f = 0$. Introducing $\bar{a}_\alpha = a_\alpha^m / v^f = -a_\alpha^f / v^m$, the fluctuation of the stretch tensor in the fibres and the matrix can be expressed as

$$\tilde{\boldsymbol{H}}_R = \begin{cases} v^f \bar{a}_\alpha \boldsymbol{M}_\alpha & \text{in } B_0^m \\ -v^m \bar{a}_\alpha \boldsymbol{M}_\alpha & \text{in } B_0^f, \end{cases} \tag{20}$$

$$\delta\tilde{\boldsymbol{H}}_R = \begin{cases} v^f \boldsymbol{M}_\alpha \delta\bar{a}_\alpha & \text{in } B_0^m \\ -v^m \boldsymbol{M}_\alpha \delta\bar{a}_\alpha & \text{in } B_0^f \end{cases} \tag{21}$$

The HM-condition (14) may now be specialised as

$$\begin{aligned} \delta\bar{\boldsymbol{U}} : \bar{\boldsymbol{T}} &= \delta\bar{\boldsymbol{U}} : \left(v^m \boldsymbol{T}^m + v^f \boldsymbol{T}^f\right) + v^m \delta\tilde{\boldsymbol{H}}_R^m : \boldsymbol{T}^m \\ &\quad + v^f \delta\tilde{\boldsymbol{H}}_R^f : \boldsymbol{T}^f \\ &= \delta\bar{\boldsymbol{U}} : \left(v^m \boldsymbol{T}^m + v^f \boldsymbol{T}^f\right) \\ &\quad + v^f v^m \boldsymbol{M}_\alpha : (\boldsymbol{T}^m - \boldsymbol{T}^f)\delta\bar{a}_\alpha \end{aligned} \tag{22}$$

We thus conclude that the stress continuity conditions in the transverse–longitudinal plane are

$$\boldsymbol{M}_\alpha : (\boldsymbol{T}^m - \boldsymbol{T}^f) = 0, \qquad \alpha \in \{22, 33, 12, 13\} \tag{23}$$

which yields the homogenised macroscale stress as

$$\bar{\boldsymbol{T}} = v^m \boldsymbol{T}^m + v^f \boldsymbol{T}^f, \tag{24}$$

from which the homogenised Cauchy stress can be calculated as

$$\bar{\boldsymbol{\sigma}} = \frac{1}{\bar{J}} \bar{\boldsymbol{R}} \cdot \bar{\boldsymbol{T}} \cdot \bar{\boldsymbol{F}}^\top, \tag{25}$$

where $\bar{\boldsymbol{F}} = \bar{\boldsymbol{R}} \cdot \bar{\boldsymbol{U}}$ is the macroscale deformation gradient and $\bar{J} = \det(\bar{\boldsymbol{F}})$.

3.3. Constituent material models

The constitutive relations are given via the stored free-energy density functions for the constituents. The *fibres* are modelled using transversely isotropic strain invariants. The total free energy function reads

$$\psi^f = \psi_v^f + \psi_d^f + \psi_a^f + \psi_s^f + \psi_P^f, \tag{26}$$

where the individual terms are detailed below.

The first two terms, ψ_v^f and ψ_d^f, are the isotropic contributions to the total strain energy, namely, the volumetric and deviatoric parts, defined as

$$\psi_v^f = \frac{1}{2} K^f \left(\boldsymbol{I} : \boldsymbol{E}^f\right)^2, \quad \psi_d^f = G^f \boldsymbol{E}_d^f : \boldsymbol{E}_d^f, \tag{27}$$

where $\boldsymbol{E}_d^f = \boldsymbol{E}^f - \frac{1}{3}\left(\boldsymbol{I} : \boldsymbol{E}^f\right)\boldsymbol{I}$ is the deviatoric part of the Green–Lagrange strain tensor, K^f is the bulk modulus, and G^f is the (isotropic) shear modulus of the fibres.

The remaining three energy contributions are connected to transverse isotropic invariants, as they involve the structure tensor $\boldsymbol{M}_{11}$ defined via the fibre orientation. ψ_a^f is the energy associated with longitudinal normal strains defined as

$$\psi_a^f = \frac{1}{2} E_L^f \left(\boldsymbol{M}_{11} : \boldsymbol{E}^f\right)^2, \tag{28}$$

where E_L^f is (approximately) the longitudinal tensile modulus of the fibres.

The term ψ_s^f refers to the energy associated with longitudinal shear

$$\psi_s^f = G_s^f \boldsymbol{E}_s^f : \boldsymbol{E}_s^f, \tag{29}$$

where the longitudinal shear strain, according to Larsson et al. (2018), is given by $\boldsymbol{E}_s^f = \boldsymbol{M}_{11} \cdot \boldsymbol{E}^f + \boldsymbol{E}^f \cdot \boldsymbol{M}_{11} - 2\left(\boldsymbol{M}_{11} : \boldsymbol{E}^f\right)\boldsymbol{M}_{11}$, and the shear modulus in the isotropy plane manifests itself as the sum of the shear stiffnesses $G^f + G_s^f$. Finally, to properly account for the Poisson effect between longitudinal and transverse normal strains, ψ_P^f is introduced as

$$\psi_P^f = \frac{1}{2} E_v^f \boldsymbol{E}_{LT}^f : \boldsymbol{E}_{LT}^f \tag{30}$$

where E_v^f is a constant that expresses the Poisson coupling of longitudinal and transverse normal strains, and $\boldsymbol{E}_{LT}^f = \left(\left(\boldsymbol{I} - \boldsymbol{M}_{11}\right) : \boldsymbol{E}^f\right)\boldsymbol{M}_{11} + \left(\boldsymbol{M}_{11} : \boldsymbol{E}^f\right)\left(\boldsymbol{I} - \boldsymbol{M}_{11}\right)$.

The total stiffness, defined as $\mathbb{C}^f = \frac{\partial^2 \psi^f}{\partial (\boldsymbol{E}^f)^2}$ in Voigt form, reads

$$\underline{\mathbb{C}}^f = \begin{bmatrix} C_{LL}^f & C_{LT}^f & C_{LT}^f & 0 & 0 & 0 \\ C_{LT}^f & C_{TT}^f & C_{TT'}^f & 0 & 0 & 0 \\ C_{LT}^f & C_{TT'}^f & C_{TT}^f & 0 & 0 & 0 \\ 0 & 0 & 0 & G^f + G_s^f & 0 & 0 \\ 0 & 0 & 0 & 0 & G^f & 0 \\ 0 & 0 & 0 & 0 & 0 & G^f + G_s^f \end{bmatrix} \tag{31}$$

with $C_{LL}^f = E_L^f + K^f + \frac{4}{3}G^f$, $C_{LT}^f = K^f - \frac{2}{3}G^f + E_v^f$, $C_{TT}^f = K^f + \frac{4}{3}G^f$, and $C_{TT'}^f = K^f - \frac{2}{3}G^f$. Equating the resulting stiffness with the small-strain transversely isotropic stiffness matrix expressed in Voigt form as

$$\underline{\mathbb{C}}^f = \begin{bmatrix} \frac{1}{E_1^f} & -\frac{\nu_{12}^f}{E_1^f} & -\frac{\nu_{12}^f}{E_1^f} & 0 & 0 & 0 \\ -\frac{\nu_{12}^f}{E_1^f} & \frac{1}{E_2^f} & -\frac{\nu_{23}^f}{E_2^f} & 0 & 0 & 0 \\ -\frac{\nu_{12}^f}{E_1^f} & -\frac{\nu_{23}^f}{E_2^f} & \frac{1}{E_2^f} & 0 & 0 & 0 \\ 0 & 0 & 0 & \frac{1}{G_{12}^f} & 0 & 0 \\ 0 & 0 & 0 & 0 & \frac{2(1+\nu_{23}^f)}{E_2^f} & 0 \\ 0 & 0 & 0 & 0 & 0 & \frac{1}{G_{12}^f} \end{bmatrix}^{-1} \tag{32}$$

we find the following relations between the classical engineering constants and the model parameters:

$$K^f = \frac{E_2^f}{6}\left(\frac{3E_1^f}{E_1^f(1-\nu_{23}^f) - 2E_2^f(\nu_{12}^f)^2} - \frac{1}{1+\nu_{23}^f}\right) \tag{33a}$$

$$G^f = \frac{E_2^f}{2(1+\nu_{23}^f)} \tag{33b}$$

$$E_L^f = \frac{(E_1^f)^2(1-(\nu_{23}^f)^2) - E_1^f E_2^f + (E_2^f \nu_{12}^f)^2}{\left(E_1^f(1-\nu_{23}^f) - 2E_2^f(\nu_{12}^f)^2\right)(1+\nu_{23}^f)} \tag{33c}$$

$$G_s^f = G_{12}^f - \frac{E_2^f}{2(1+\nu_{23}^f)} = G_{12}^f - G_{23}^f \tag{33d}$$

$$E_v^f = \frac{E_2^f\left(E_1^f((1-\nu_{12}^f)\nu_{23}^f - \nu_{12}^f) + E_2^f(\nu_{12}^f)^2\right)}{\left(2E_2^f(\nu_{12}^f)^2 - E_1^f(1-\nu_{23})\right)(1+\nu_{23}^f)} \tag{33e}$$

We note that if $E_2 \ll E_1$, then $E_L^f \approx E_1^f$. The second Piola–Kirchhoff stress tensor in the fibre material can be obtained from the strain energy density function as

$$\boldsymbol{S}^f = \frac{\partial \psi^f}{\partial \boldsymbol{E}^f} = \mathbb{C}^f : \boldsymbol{E}^f. \tag{34}$$

An isotropic *matrix* response is assumed, and material nonlinearities in compression/shear are modelled by continuum damage mechanics that degrade the deviatoric part of the stored free energy density function defined as

$$\psi^m = f[d]\, G^m \boldsymbol{E}_d^m : \boldsymbol{E}_d^m + \frac{1}{2} K^m (\boldsymbol{I} : \boldsymbol{E}^m)^2, \tag{35}$$

where $0 \le d \le 1$ is the damage variable, G^m the initial shear modulus, K^m the bulk modulus of the effective matrix material, $\boldsymbol{E}_d^m$ the deviatoric part of the Green–Lagrange strain tensor defined as $\boldsymbol{E}_d^m = \boldsymbol{E}^m - \frac{1}{3}(\boldsymbol{I} : \boldsymbol{E}^m)\boldsymbol{I}$. Furthermore, $f[d] = (1-d)^2$ is a function representing material degradation in the matrix. A quadratic degradation term is adopted here, consistent with the standard AT2 phase-field formulation (Mandal et al., 2019). Strain rate dependency and plasticity have been observed in unidirectional CFRPs with both thermoplastic and thermoset matrices (Ma et al., 2021; Wang et al., 2018; Fallahi et al., 2019). As these features have not been included in the current model

Table 1
Elastic properties of IM7 fibres and 8552 matrix from the WWFE-III (Kaddour et al., 2013b).

E_1^f GPa	E_2^f GPa	ν_{12}^f	ν_{23}^f	G_{12}^f GPa	G^m GPa	K^m GPa
276	19	0.2	0.357[a]	27	1.478	5.667[b]

[a] Calculated as $\nu_{23}^f = \frac{E_2^f}{2G_{23}^f} - 1$.

[b] Calculated as $K^m = \frac{E^m}{3(1-2\nu^m)}$.

Table 2
IM7/8552 UD laminate strengths and fibre volume fraction from the WWFE-III (Kaddour et al., 2013b).

X_c MPa	Y_c MPa	S_{12} MPa	v^f %
1590	185	90	60

formulation, its usage is limited to monotonic quasi-static loading scenarios, where plasticity is mimicked by damage.

The second Piola–Kirchhoff stress tensor in the matrix material can be obtained from the strain energy density function as

$$\boldsymbol{S}^m = \frac{\partial \psi^m}{\partial \boldsymbol{E}^m} = 2f[d]G^m \boldsymbol{E}_d^m + K^m E_v^m \boldsymbol{I}. \tag{36}$$

To introduce damage evolution, we define a rate-dependent damage potential in the matrix as

$$\phi = \phi^s - \frac{G_c}{v^*}\dot{d} \quad \text{with } \phi^s = A - \frac{G_c}{l_d} d \tag{37}$$

where G_c is the critical shear strain energy release rate, l_d is the length scale of the diffuse fracture area, and v^* is the fracture area progression speed parameter. Furthermore, the damage driving force A is defined as

$$A = -\frac{\partial \psi^m}{\partial d} = -f'[d]\, G^m \boldsymbol{E}_d^m : \boldsymbol{E}_d^m \geq 0 \tag{38}$$

With the polynomial damage degradation function defined above, we find that $f'[d] = -(1-d)$.

Progressive damage is governed by the Karush–Kuhn–Tucker conditions defined as $\phi \leq 0$, $\dot{d} \geq 0$, $\phi \dot{d} = 0$. To satisfy these conditions, we propose a simple Bingham law for damage evolution

$$\dot{d} = \frac{v^*}{G_c}\langle \phi^s \rangle = \frac{v^*}{l_d}\langle d^s - d \rangle, \tag{39}$$

where $\langle \bullet \rangle$ is used here as Macaulay brackets, defined as $\langle \bullet \rangle = \max(\bullet, 0)$. In the last equality, we introduce the "inviscid" case $v^* \to \infty$ corresponding to $\phi^s = 0$ where static damage d^s is

$$d^s = \frac{A\, l_d}{G_c} \geq 0. \tag{40}$$

4. Applications

4.1. Uniaxial compression and shear tests of UD plies

The three World-Wide Failure Exercises (WWFEs) were organised to obtain an objective, extensive comparison between the various failure theories of polymer matrix composites. Data from the WWFE-III were used here to assess the predictive capability of the presented model in uniaxial load cases and to investigate the predicted final failure envelopes in in-plane biaxial load cases. For this study, experimental data from an IM7/8552 composite system were used, available in Kaddour et al. (2013b). The constituent properties are summarised in Table 1 and the ply properties in Table 2.

Virtual uniaxial and pure shear stress tests of unidirectional laminates were performed at the material point level using the elastic properties of the constituents presented in Table 1. The critical strain energy release rate G_c in the matrix damage model was chosen as the strain energy release rate of the composite in Mode II, representative of shear failure, which is expected at the micro level in the load cases investigated.

Table 3
Damage evolution parameters of the matrix material calibrated based on the transverse compressive strength.

G_c mJ/mm^2	l_d mm	v^* mm/s
0.8	0.012	0.1

The xyz coordinates are chosen such that the z direction is normal to the laminate's plane, and x denotes the nominal longitudinal direction. For the calculation, we consider the deformation gradient relative to the xyz coordinates restricted to the form

$$\bar{\boldsymbol{F}} = \begin{bmatrix} \bar{F}_{xx} & \bar{F}_{xy} & 0 \\ 0 & \bar{F}_{yy} & 0 \\ 0 & 0 & \bar{F}_{zz} \end{bmatrix}. \tag{41}$$

For the LS-F_{21} longitudinal shear case (see Fig. 5), the shear deformation is transverse to the fibres, and the deformation gradient is

$$\bar{\boldsymbol{F}} = \begin{bmatrix} \bar{F}_{xx} & 0 & 0 \\ \bar{F}_{yx} & \bar{F}_{yy} & 0 \\ 0 & 0 & \bar{F}_{zz} \end{bmatrix}. \tag{42}$$

During loading, a component of the deformation gradient is prescribed: $\bar{F}_{xx}$ for longitudinal compression, $\bar{F}_{yy}$ for transverse compression, and $\bar{F}_{xy}$ or $\bar{F}_{yx}$ for shear.

The uniaxial/biaxial stress state conditions were considered in terms of the Cauchy stress in uniaxial longitudinal compression, transverse compression, and pure shear stress states, respectively, as

$$\bar{\boldsymbol{\sigma}}_L = \begin{bmatrix} \bar{\sigma}_{xx} & 0 & 0 \\ 0 & 0 & 0 \\ 0 & 0 & 0 \end{bmatrix}, \quad \bar{\boldsymbol{\sigma}}_T = \begin{bmatrix} 0 & 0 & 0 \\ 0 & \bar{\sigma}_{yy} & 0 \\ 0 & 0 & 0 \end{bmatrix}, \quad \bar{\boldsymbol{\sigma}}_S = \begin{bmatrix} 0 & \bar{\sigma}_{xy} & 0 \\ \bar{\sigma}_{xy} & 0 & 0 \\ 0 & 0 & 0 \end{bmatrix} \tag{43}$$

and the corresponding combination of nonzero elements in biaxial loading. The unprescribed components in the deformation gradient are obtained such that the restrictions on the stress tensor are fulfilled.

The length and speed parameters l_d and v^* of the damage evolution law (39) were calibrated based on the transverse uniaxial compressive curve from WWFE-III (Kaddour et al., 2013a), corresponding to the parameters summarised in Table 3. The nominal compressive strain rate used for the calibration was 0.04 1/s, and Fig. 4 shows the measured and simulated results from the uniaxial test. Here, the last experimental data point used for calibration corresponds to the highest stress prior to failure, whereas the CDM model describes a smooth transition from ductile pre-peak behaviour to softening post-peak failure behaviour. We also included the evolution of the damage variable d responsible for the ductile degradation in Fig. 4. However, there is generally even higher ductility in the experimental curve compared to what could be achieved with the present CDM model. This may be explained by inelastic deformation coupled with damage in the matrix material. We also note that good agreement was obtained for the initial modulus, although no calibration was made concerning the elastic response in this test.

For validation, the nonlinear CDM model was then applied to the two longitudinal shear tests (LS-F_{12} and LS-F_{21}), both in a pure shear stress state, using calibrated parameters at a strain rate similar to that used in transverse compression. The different test cases are explained in Fig. 5, and the resulting CDM model shear curves are shown in Fig. 6. The measured shear strength was 90 MPa, and the predicted values from the homogenised model are 100.8 MPa and 101.8 MPa in the LS-F_{21} and LS-F_{12} cases, respectively. The difference between the

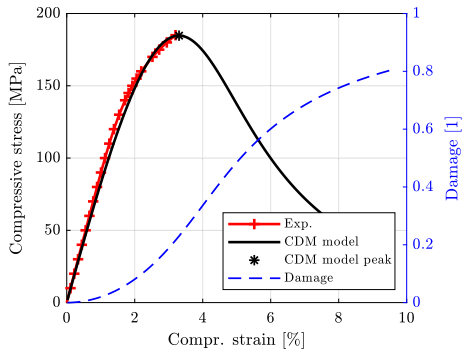

Fig. 4. Experimental and calibrated model response for uniaxial transverse compression. The experimental data are from the WWFE-III.

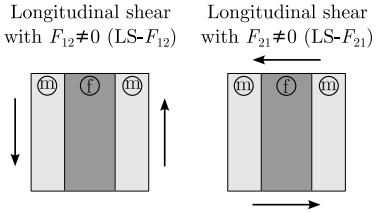

Fig. 5. Schematic representation of the prescribed deformation components used to obtain a pure shear Cauchy stress. The arrows show the direction of prescribed nonzero shear component in the deformation gradient, meanwhile the perpendicular shear is zero. ⓕ — fibre, ⓜ — matrix.

experimental and simulated shear strength is 12.0% and 13.1% in the two cases. The evolution of damage in the simulations is also shown, which coincides for the two cases (LS-F_{21} and LS-F_{12}).

As apparent in Fig. 6, the model underestimates the initial experimental tangent shear modulus. For small strains, the Biot stress is $\boldsymbol{T} \approx \boldsymbol{\sigma}$, and therefore, Eqs. (23) and (24) apply to the components of the Cauchy stress. In longitudinal shear, i.e., when $\alpha = 12$ in Eq. (23), the conditions are $\sigma_{12}^m = \sigma_{12}^f$ and $v^m \sigma_{12}^m + v^f \sigma_{12}^f = \bar{\sigma}_{12}$ of the first order. As expected, the initial (small strain) shear modulus of the CDM model corresponds to the lower bound shear stiffness of the Reuss model, where the effective composite modulus is $G_{12} = (v^m/G^m + v^f/G_{12}^f)^{-1}$.

The semi-empirical Halpin–Tsai method (Affdl and Kardos, 1976) with parameter $\zeta_{\bar{G}} = 1$ provides a better prediction of the homogenised elastic shear modulus; however, it does not carry information about the nonlinear part of the curve and thus does not provide information about the shear strength. We also note that when calibrating the damage parameters of the CDM model, no information about the shear curve or shear strength was used; it is purely an outcome of the constituent elastic properties and the calibration performed on the transverse strength, as displayed in Fig. 4.

Furthermore, there is a discrepancy in the nonlinear shape of the shear curves of the (elastic shear induced) CDM model and the shear experiment. A possible remedy is to extend the model; for example, by incorporating elastoplasticity at the cost of additional model parameters.

We highlight that the nonlinear response of the matrix is calibrated based on the transverse compressive curve without the consideration of any fibre misalignment. By decoupling the effects of the nonlinearity of the matrix and geometric imperfection the calibration process is simplified.

In a second step, the 1 axis is slightly misaligned by the in-plane rotation angle $\theta_i := \varphi_0$ from the global x axis, along which uniaxial compression is applied, to trigger fibre kinking behaviour. The initial fibre misalignment angle is calibrated against the measured compressive strength X_c; a good match was found for $\varphi_0 = 1.314°$. The

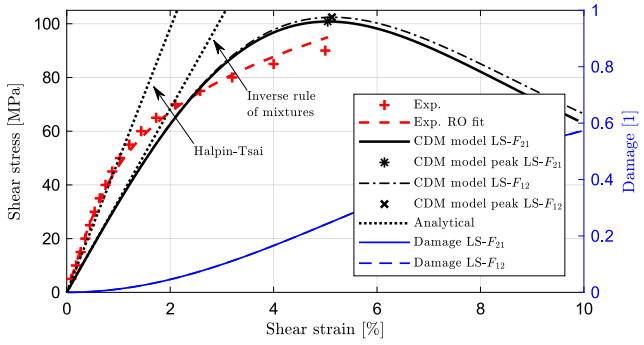

Fig. 6. Experimental and calibrated model shear responses, Ramberg–Osgood curve fitted to experimental data, and analytical initial shear modulus predictions. The experimental data are from the WWFE-III. The last experimental data point corresponds to the in-plane shear strength.

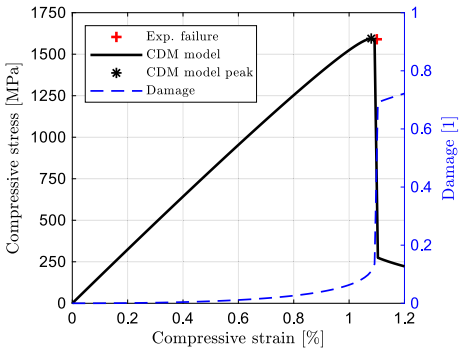

Fig. 7. Experimental and calibrated model response for uniaxial longitudinal compression with an in-plane misalignment angle of $\varphi_0 = 1.314°$. The experimental data are from the WWFE-III. The longitudinal strain is calculated as $\bar{F}_{xx} - 1$.

corresponding longitudinal (misaligned) compressive fibre response is shown in Fig. 7.

Budiansky and Fleck (1993) provided a closed-form solution for the compressive strength of a composite with a nonlinear shear response governed by a Ramberg–Osgood law. The shear stress–strain relationship can be written as

$$\gamma_{12} = \frac{1}{G_{12}} \left(\sigma_{12} + \text{sign}(\sigma_{12})\, \alpha\, |\sigma_{12}|^{\eta} \right), \tag{44}$$

and the compressive strength with an initial fibre misalignment of φ_0 is

$$X_c = \frac{G_{12}}{1 + \eta\, \alpha^{1/\eta} \left(\frac{G_{12}\varphi_0}{\eta - 1} \right)^{\frac{\eta-1}{\eta}}}. \tag{45}$$

Since X_c is easier to measure than φ_0, Eq. (45) is more commonly used to calibrate φ_0 in models. Rearranging Eq. (45), we arrive at

$$\varphi_0 = \frac{\eta - 1}{G_{12}} \left(\frac{1}{\eta\, \alpha^{1/\eta}} \left(\frac{G_{12}}{X_c} - 1 \right) \right)^{\frac{\eta}{\eta-1}}. \tag{46}$$

A Ramberg–Osgood expression was fitted to the experimental curve, represented by the dashed red curve in Fig. 6, which was used to calculate the initial misalignment angle according to the fibre kinking theory (FKT). The parameters fitted against the experimental shear test of the Ramberg–Osgood curve shown in Fig. 6 are $G_{12} = 5.99$ GPa, $\alpha = 2.99 \cdot 10^{-6}$, and $\eta = 3.96$. The initial misalignment angle is 1.28° according to Eq. (46), from which the angle obtained with the model by fitting to the longitudinal strength differs only by 2.6%.

A more ductile response can be observed in transverse compression and shear, as is apparent from the evolution of damage and the smooth

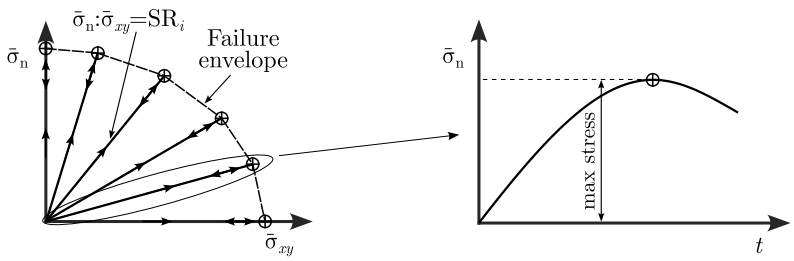

Fig. 8. The procedure of generating failure envelopes with the model presented. (a) Biaxial failure data points and interpolation, (b) maximum stress detection for a given stress ratio.

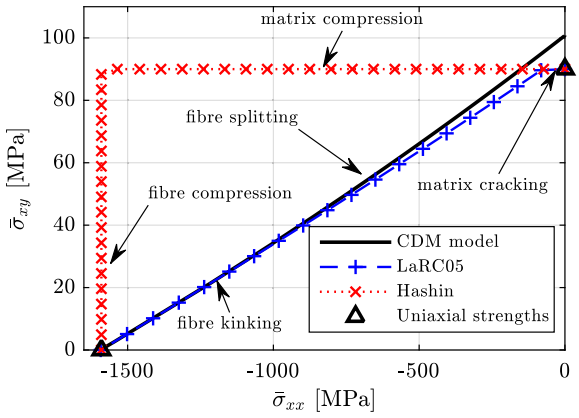

Fig. 9. Maximum stress envelope under combined longitudinal compression and in-plane shear in comparison with failure envelopes of analytical failure models.

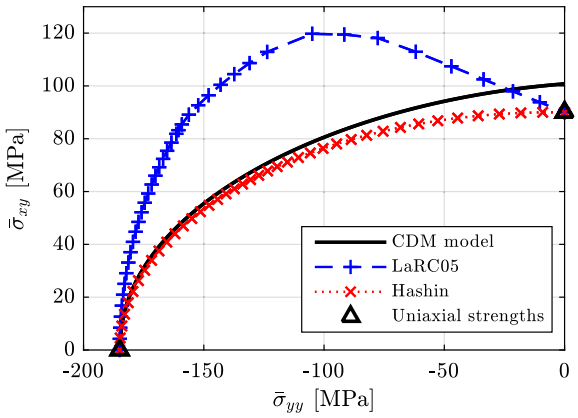

Fig. 10. Maximum stress envelope under combined in-plane transverse compression and in-plane shear in comparison with failure envelopes of analytical failure models.

transition to softening in the stress–strain curves. However, under longitudinal compression in Fig. 7, there is a sudden increase in damage right after the compressive strength is reached, accompanied by a sharp stress drop. This non-smooth change is due to a snap-back behaviour in the stress–strain curve that is not captured by the current deformation gradient-driven solver.

4.2. Failure envelope of UD plies in in-plane biaxial stress states

In this section, we relate the proposed nonlinear CDM model response for a composite ply to two well-known theories: the LaRC05 and Hashin ply failure criteria. To generate the failure envelopes for the CDM model in the stress plane $\bar{\sigma}_n - \bar{\sigma}_{xy}$ ($n = xx, yy$), where $\bar{\sigma}_n$ denotes the nonzero normal stress component and $\bar{\sigma}_{xy}$ the in-plane stress, we follow the procedure outlined in Fig. 8. The prescribed component of the deformation gradient is progressively increased so that the stress ratio defined as SR $= \bar{\sigma}_n/\bar{\sigma}_{xy}$ remains constant and equal to a prescribed value. The process continues until the stress $\bar{\sigma}_n$ reaches its maximum value. At this point, the maximum stress is marked as the maximum reachable stress for that stress ratio. To handle the two extreme cases, SR $= 0$ and SR $= \infty$, longitudinal compression/pure shear and transverse compression/pure shear tests are considered. In these cases, we perform controlled incrementation of $\bar{F}_{xx}$ for longitudinal compression/shear and incrementation of $\bar{F}_{yy}$ for transverse compression/shear, while the out-of-plane ply stresses are zero, as well as the perpendicular in-plane normal stress ($\bar{\sigma}_{yy}$ for longitudinal compression/shear and $\bar{\sigma}_{xx}$ for transverse compression/shear).

Figs. 9 and 10 show the model response as failure envelopes generated with the loading procedure. The envelope in Fig. 9 shows the longitudinal compression/shear $\bar{\sigma}_{xx} - \bar{\sigma}_{xy}$ failure envelope, and Fig. 10 shows the transverse compression/shear $\bar{\sigma}_{yy} - \bar{\sigma}_{xy}$ failure envelope. The calculated failure envelopes of the model are compared with two initial failure criteria by Hashin Hashin (1980) and LaRC05 (Pinho et al., 2012). The failure envelopes with respect to the LaRC05 and Hashin criteria are generated in a similar way to the procedure outlined in Fig. 8, but in these cases, the value of the failure index is tracked, and the failure stress state is saved when the failure index reaches the value of 1. Several additional parameters were required for the LaRC05 criterion. The fracture plane for pure transverse compression was assigned as $\alpha_0 = 53°$ as a general value for composites. The shear friction coefficients of the LaRC05 model were calculated using the ply strengths as $\eta_L = -\frac{S_{12}\cos(2\alpha_0)}{Y_C \cos^2(\alpha_0)} = 0.3702$ and $\eta_T = -\frac{1}{\tan(2\alpha_0)} = 0.2867$, and the transverse shear strength as $S_{13} = \frac{Y_c}{2\tan(2\alpha_0)} = 69.7$ MPa to match the experimentally measured transverse compressive strength. Furthermore, the initial fibre misalignment angle was calibrated to $\varphi = 2.58°$ on the longitudinal compressive strength, X_c.

In the absence of transverse stress, the Hashin failure criterion reduces to the maximum stress criterion in biaxial longitudinal compression/shear, with a fibre failure limit on the normal stress and a matrix failure limit on the shear stress. In the case of the LaRC05 criterion, the failure mode is fibre kinking/fibre splitting defined by the same equation, except in the vicinity of the pure shear stress state, where failure is caused by matrix cracking. The current model shows very good agreement with the LaRC05 model for large longitudinal compressive stresses, i.e., for fibre-kinking failure. Since $Y_c \approx 2S_{12}$, the Hashin criterion leads to Fig. 10, showing the failure envelope in combined transverse compression/shear. The mode of failure is matrix compression for the Hashin criterion and matrix cracking for the LaRC05 criterion. $S_{13} = 90$ MPa was used for the Hashin model as reported in Kaddour et al. (2013b), since its value did not influence the uniaxial strengths. The LaRC05 criterion predicts increased shear strength in the presence of moderately large transverse compressive stress due to compressive stress counteracting microcrack opening and growth. This appears in the form of a transverse stress-dependent shear

Table 4
Layup and thickness of the different laminate coupons. Layers without a superscript denote UD layers.

Laminate	Layup	Thickness [mm]
A — 0°	$[\pm 45^{\text{twill}}/0/0/\pm 45^{\text{twill}}/0]_S$	4.4
A — 45°	$[(0/90)^{\text{twill}}/45/45/(0/90)^{\text{twill}}/45]_S$	4.4
B — 0°	$[\pm 45^{\text{NCF}}/(0/90)^{\text{twill}}/\pm 45^{\text{twill}}]_S$	3.2
B — 45°	$[(0/90)^{\text{NCF}}/\pm 45^{\text{twill}}/(0/90)^{\text{twill}}]_S$	3.2
C — 0°	$[\pm 45^{\text{NCF}}/(0/90)^{\text{twill}}]_S$	1.9
C — 45°	$[(0/90)^{\text{NCF}}/\pm 45^{\text{twill}}]_S$	1.9

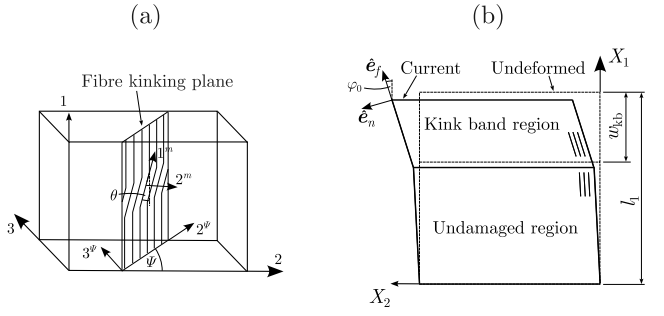

Fig. 11. (a) The bases of the fibre kinking plane and the misalignment frame in the LaRC05 criterion, reconstructed based on Pinho et al. (2006a). (b) Finite element decomposition during fibre-kinking failure in the CompDam DGD model, reconstructed based on Herraez et al. (2018). $\hat{\mathbf{E}}_f$ and $\hat{\mathbf{E}}_n$ are the fibre and normal directions in the reference configuration.

strength in the criterion, which is not considered explicitly in the formulation of the CDM model. The ultimate stress curve obtained with the CDM model qualitatively agrees well with the Hashin criterion in this load case.

4.3. Compression tests of laminated composite coupons

The CDM model is applied to quasistatic compression tests of three laminates. The test results are summarised in Andersson and Ståhl (2019). The different laminates are referenced according to Andersson and Ståhl (2019) as laminates A, B, and C, and are tested at two orientations: 0° and 45°. The layup and thickness of the laminates are summarised in Table 4. All plies are made of T700/epoxy composite; the thicknesses of the UD, NCF, and twill plies are 0.3 mm, 0.28 mm, and 0.64 mm, respectively. The untabbed gauge length and width of all investigated coupons were both 13 mm.

The experiments were simulated by Andersson and Ståhl (2019) using the material model of Pinho et al. (2006a,b). In this work, the compression response of laminates is compared using three different material models: the model of Pinho et al. (using the LaRC05 criterion for damage initiation), the NASA CompDam DGD code (Leone et al., 2019) (using fibre kinking theory and deformation gradient decomposition for longitudinal compressive failure), and the model proposed in this article.

4.3.1. Modelling fibre-kinking failure in the computational models compared

The modelling of fibre-kinking failure is treated differently in the computational model by Pinho et al. (2006a) and the CompDam DGD model (Herraez et al., 2018). A short summary of the key differences is given in this Section. An extended summary is also provided in Appendices A and B.

In the Pinho model, the LaRC05 failure criterion is used as a failure initiation criterion, where the stress state is rotated from the ply's 123 coordinate system to the misalignment frame $1^m 2^m 3^\psi$, as illustrated in Fig. 11(a). The traction vector on the (potential) fracture plane is calculated using the stress state expressed in the rotated coordinate system, and a matrix failure criterion is applied. After failure initiation, the traction vector is degraded by a damage variable so that the dissipated energy is mesh-independent. Damage degradation is initiated via a stress-based failure criterion, and damage propagation is governed by an energy-based law.

The CompDam DGD model uses a decomposition of the finite elements affected by fibre kinking into a kinked and an undamaged region, as shown in Fig. 11(b). The kink band width w_{kb} is an input parameter in the model and denotes the initial length of the kink band. The rotation of the fibres in the kink-band region can be different from that in the undamaged region; the rotation angle is obtained through a traction continuity condition. In-plane shear nonlinearity is considered via a one-dimensional plasticity model governed by the Ramberg–Osgood expression. It is also possible to model the longitudinal Young's modulus as linearly dependent on the longitudinal normal strain in the implementation. The sources of nonlinearity are therefore geometrical (sub-element level fibre rotation) and material (plastic shear nonlinearity and, optionally, nonlinear longitudinal Young's modulus).

4.3.2. Description of the finite element models

As a representative example, the mesh of laminate A — 0° is shown in Fig. 12. The finite element meshes were generated using a script provided by the authors of Andersson and Ståhl (2019). The mesh dependence of the proposed CDM model is not discussed here; however, the adopted rate dependent damage evolution model has been shown to be mesh objective when placed in a slightly different context of damage degradation, cf. Larsson et al. (2018). The plies are meshed with 8-node linear brick elements with reduced integration (C3D8R in Abaqus), using one element through the thickness for the UD plies and two elements for the NCF and twill plies. The in-plane size of the elements is 0.25 mm, following Andersson and Ståhl (2019). The constitutive models of the plies are implemented in Abaqus/Explicit using the VUMAT subroutine interface, and the interactions between plies are governed by a cohesive law-based surface contact formulation with a quadratic initiation criterion.

Compression is performed in the global x direction, with one side constrained in the x direction, one vertical edge fixed in the vertical direction, and one horizontal edge fixed in the horizontal direction, as shown in Fig. 12. The other side was moved with a predefined velocity of $v = 10$ mm/s, with a smooth transition from $v = 0$ mm/s to $v = 10$ mm/s to avoid the generation of elastic waves in the simulation. The ENHANCED option was used for hourglass control and variable mass scaling with a stable target time step size of 10^{-6} s. Under the above conditions, the kinetic energy and the artificial strain energy were found to be negligible compared to the internal energy.

To avoid damage initiation on the end faces where boundary conditions are prescribed, two 2.5 mm purely elastic sections are defined at the two ends of the coupon, as shown in Fig. 12. Element deletion was applied for the present CDM model with a limit of 95% matrix damage.

All material models considered here are established for UD plies. Therefore, NCF and twill plies are modelled as [0/90] UD laminates with adjusted material parameters. It can be seen in Fig. 12 that two layers of elements represent a single [±45] twill ply, one oriented at +45° and one at -45°.

For interlaminar behaviour, delamination is controlled by surface contacts based on a cohesive law. The parameters of the cohesive zone model are summarised in Table 5. We note that the nodes on the artificial surfaces created in the mid-plane of the twill fabrics and stacked UD plies, where there is no physical delamination, are bound together. As reported in Andersson and Ståhl (2019), thermoplastic threads were used to stitch the 0° and 90° plies together in the NCF fabrics, which melt during the processing of the material, making internal delamination possible. The same parameters reported in Table 5 were used to model the internal delamination of NCF plies. At surface contacts, where delamination is possible, a cohesive zone model is defined with an initial gap of 0.1 μm in the mesh between plies.

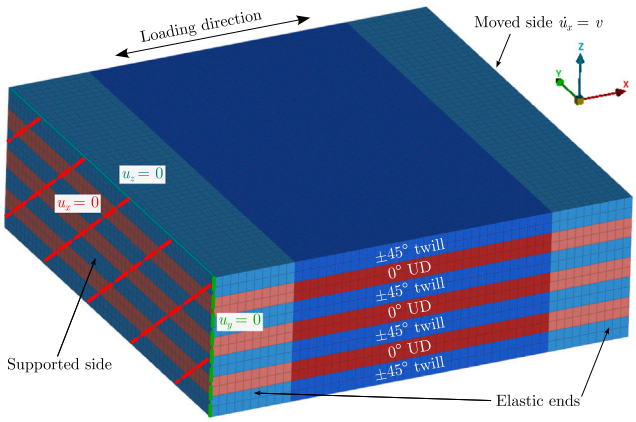

Fig. 12. Finite element mesh and boundary conditions of Laminate A — 0°.

Table 5
Parameters of the cohesive zone contact behaviour modelling delamination, Dassault Systèmes (2024). The index n denotes normal, s shear and t tangential directions.

	Parameter	Value
Contact stiffnesses	K_{nn}	10^6 N/mm^3
	K_{ss}	10^6 N/mm^3
	K_{tt}	10^6 N/mm^3
Interfacial strengths	t_n^0	60 MPa
	t_s^0	90 MPa
	t_t^0	90 MPa
Critical fracture energies	G_n^C	0.2 N/mm
	G_s^C	0.8 N/mm
	G_t^C	0.8 N/mm
BK[a] mixed mode power coefficient	η	1.75

[a] Benzeggagh–Kenane.

Table 6
Elastic properties of T700 fibres (Truong et al., 2005) and LY556 matrix (Kaddour et al., 2013b).

E_1^f GPa	E_2^f GPa	ν_{12}^f	ν_{23}^f	G_{12}^f GPa	E^m GPa	ν^m
270	28	0.23	0.07	50	3.35	0.35

4.3.3. Material parameter calibration

The calibration of material parameters concerns the CompDam DGD model and the present CDM model, whereas the parameters for the model of Pinho et al. are taken from Andersson and Ståhl (2019).

The elastic ply properties reported in Andersson and Ståhl (2019) were used for the CompDam DGD model. Furthermore, the feature flags 0404000 were applied (see Leone et al. (2019) for their detailed meaning), indicating that matrix cracking is not considered and fibre kinking is only accounted for in the out-of-plane direction. The reason for excluding matrix cracking is convergence problems when both matrix cracking and fibre kinking are active. The width of the kink band, w_{kb}, which is used for the deformation gradient decomposition procedure, is set to 100 μm.

In simulations using the present CDM model, the elastic properties of the T700 fibres reported in Truong et al. (2005) were used. Due to the lack of experimental data available on pure resin, the elastic properties of LY556 resin reported in Kaddour et al. (2013b) were assumed. The elastic properties are summarised in Table 6. Furthermore, a fibre volume fraction of 57% was assumed.

Using the proposed CDM model in a coupon test simulation, the initial fibre misalignment distribution is considered by mapping the local fibre direction at the integration points. As this information on the specimens was not available, an equivalent misalignment angle was applied in the middle of the 0° plies according to Fig. 13. In the present paper, we made the pragmatic assumption to misalign one row of elements of the UD and NCF plies and two rows of elements of the twill plies. The misalignment was assumed to be in the out-of-plane direction, and its value was calibrated on the compressive strength of simple laminates made of the same type of plies, as explained later in the Section. This strategy tacitly assumes that the kink band width is equal to the element size in the longitudinal direction of the 0° plies, unlike in models with distributed defects where the kink band width is an input parameter.

Out-of-plane kinking was assumed, as this is the generally observed failure mode for unidirectional laminates under longitudinal loading (Fleck et al., 1997; Wilhelmsson et al., 2020). This is also the expected failure mode in the [0/90] NCF and twill plies due to the fabrics' architecture. The assumption is also in line with the information about the experimentally observed failure modes reported in Andersson and Ståhl (2019).

We emphasise that the calibration procedure of the equivalent initial misalignment angle differs conceptually from the fibre kinking theory, and is based on the measured compressive strength of the ply. Several initial misalignment patterns were investigated, including homogeneous and normally distributed fibre misalignments; however, the chosen strategy showed the most promising results and was retained for the remainder of the analysis. Introducing an initial misalignment in every finite element of the entire specimen triggered global instability of the sample and random misalignments following a normal distribution resulted in some elements having unreasonably high misalignment angles at the compressive strength of the plies.

The misalignment of two rows of elements in opposite directions was motivated by imitating the crimped nature of the woven layers. For the ±45° and 90° plies, the nominal fibre direction is used throughout the ply. Certainly, the approach adopted for misaligned fibres is delicate. One consequence is that the fracture plane tends to orient perpendicular to the longitudinal direction, despite experiments indicating that the fracture plane is often oriented at a non-zero angle to the longitudinal direction; see e.g. Kabiri Ataabadi et al. (2014) for kink band failure in unidirectional laminates and Pinho et al. (2006c) for multidirectional laminates.

Material parameter calibration has been performed for the nonelastic parameters and initial misalignment in the CDM and CompDam DGD models. For the CDM model, the damage law parameters were calibrated on the transverse compressive curve of a $[90]_{10}$ UD laminate. The response with calibrated parameters ($G_c = 2.188$ mJ/mm^2, $v^* = 6410$ mm/s, and $l_d = 0.0488$ mm) is shown in Fig. 15b. The experimental pre-peak response shows ductile behaviour originating from inelastic deformation in the matrix. This is not entirely captured by the current CDM model, where the source of nonlinearity is elastic damage in the matrix. Extending the behaviour of the matrix with plasticity coupled to damage is a possible remedy to improve the ductile transverse compressive response. Unlike the present CDM model, the CompDam DGD model exhibits a linear elastic response to brittle failure, without any nonlinearities.

The initial out-of-plane fibre misalignments for the different plies, considered as material parameters for the CompDam DGD code and as rotations of the material coordinate system for the CDM model, were calibrated on the compression curves of $[0]_{10}$, $[(0/90)^{\text{NCF}}]_{10}$, and $[(0/90)^{\text{twill}}]]_4$ laminates. In each laminate, the average strength used for calibration was based on five experimental curves. Longitudinal compressive failure according to the CompDam DGD model is controlled by a nonlinear shear curve described by the Ramberg–Osgood law. The shear curves were measured on UD Iosipescu specimens, and the same Ramberg–Osgood shear curve was assumed for all types of plies (UD, NCF, and twill). The range of experimental curves and the fitted Ramberg–Osgood law are shown in Fig. 14. The calibrated Ramberg–Osgood parameters are $\alpha_{\text{PL}} = 3.24 \cdot 10^{-9}$ and $n_{\text{PL}} = 5.8345$. The measured and simulated calibrated compressive curves are shown in Fig. 15,

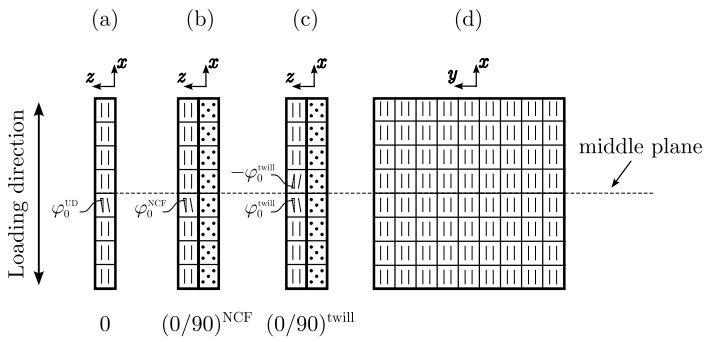

Fig. 13. Initial fibre orientation using the present CDM model. (a) Side view of a 0 UD ply, (b) side view of a [0/90] NCF ply, (c) side view of a [0/90] twill ply, (d) top view of any 0 degree ply.

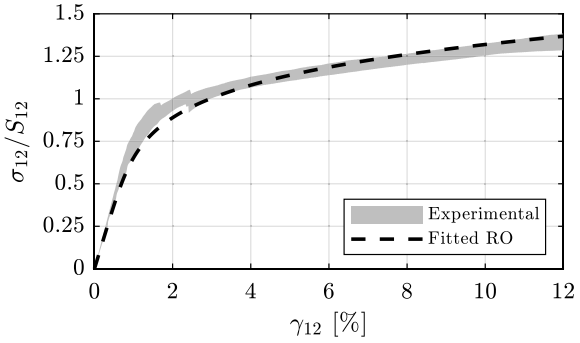

Fig. 14. Range of experimental shear curves and fitted Ramberg–Osgood curve.

Table 7
Initial fibre misalignment angles for the different models and ply types.

Model	Initial misalignment angle			Source
	UD	NCF	Twill	
Present CDM model	6.8°	11.2°	16.3°	Calibrated
CompDam DGD	6.19°	3.55°	3.95°	Calibrated
Pinho et al.	4.5°	5°	5.5°	From Andersson and Ståhl (2019)

and the calibrated initial fibre misalignment angles are in Table 7. It appears that UD plies have the largest calibrated initial misalignment angle for the CompDam DGD code. This contrasts with the present CDM model and the model of Pinho et al. where UD plies have the smallest initial misalignment, which aligns with our expectations. The calibrated initial misalignment angles differ significantly for the NASA CompDAM DGD code and the present CDM model for NCF and twill plies. This is partly attributed to the differences in modelling the initial geometrical imperfection and its time evolution. The NASA CompDam DGD code considers only part of the element to be misaligned, according to the kink band width w_{kb}. Furthermore, the rotation of the fibres in the kink band is different from the rotation of the finite element; it is calculated by subdividing the finite element into an undamaged region and a kink band region. In contrast, in the CDM model, the kink band width is given by the element size in the longitudinal direction, and the rotation of the fibres is the same as the rotation of the 1 axis of the finite element.

The localised failure modes of the virtual coupons using the CDM model are shown in Fig. 16. For longitudinal compression tests, the fracture surface is always perpendicular to the loading direction induced by the fibre misalignment, while in transverse compression, a pure 45° out-of-plane shear failure mode is obtained.

4.3.4. Model response comparison

A model response comparison is conducted for compressive experimental measurements. Three experiments were performed on laminates A, B, and C in 0° and 45° orientations. The experimental curves and the validation simulations using the calibrated material parameters are shown in Fig. 17. As a main result, the CDM model was able to capture the main qualitative characteristics of the curves, although the prediction of the ductile response of 45° off-axis loaded Laminate A is not as accurate as that of Laminates B and C.

Fig. 18 shows the virtual deformed coupons along with the damage field at failure using the present CDM model. The first ply failure is fibre kinking in every simulation, initiating in the 0° plies. Although damage propagates through the plies, significant damage can also be observed in the 45° and 90° plies. However, the damage process is concentrated mainly in the middle of the specimen, where the initial fibre misalignment is applied. A more detailed discussion of the different model behaviours is as follows.

A significant decrease in stiffness is observed in the early elastic region with the NASA CompDam DGD code under compression of the $[0]_{10}$ UD laminate and laminate A — 0°, where the stiffness of the laminates is governed by the 0° UD plies. This is due to the rotation of the fibres in the kink band region that is present in the element from the beginning. The calibrated misalignment angle of the UD plies with the NASA CompDam DGD code is 6.8°. This misalignment angle is significantly higher than the angle in the 0° plies of NCF and the twill plies (3.55° and 3.95°), which explains the pronounced loss of stiffness for the 0° UD plies. The present CDM model also showed a small decrease in stiffness with increasing strains (see Laminate A - 0° in Fig. 18) compared to the model of Pinho et al. that is linear in the elastic region, but the loss of stiffness is less prominent and the predicted curve is more in line with the experiments in which some loss of stiffness is also observed. No significant loss of stiffness is observed in the early elastic region of the simulated responses with any of the models in the laminates where the 0° layer is not a UD layer. In laminate A — 45°, there are many 45 and 90 layers and only a few 0 layers, which resulted in a more ductile experimental response with high nonlinearity starting in the early elastic range, which none of the computational models was able to capture. In laminate B — 0°, the present CDM model predicted a brittle failure at the ultimate stress, as observed in the three experiments. The stress dropped more gradually with the model of Pinho et al. and the first peak stress was followed by further hardening with the NASA CompDam DGD code. In two of the three experiments of laminate B — 45°, the first peak was followed by a short softening and then a prolonged hardening region followed by a brittle failure. This process was well reproduced qualitatively with the current CDM model as well as by the NASA CompDam DGD code, although convergence issues occurred before the stress drop in the latter case. However, the model of Pinho et al. did not predict any hardening after the first peak load. For laminate C — 0°, the first peak load is approximately the same for the present CDM model and the model of Pinho et al. After the first

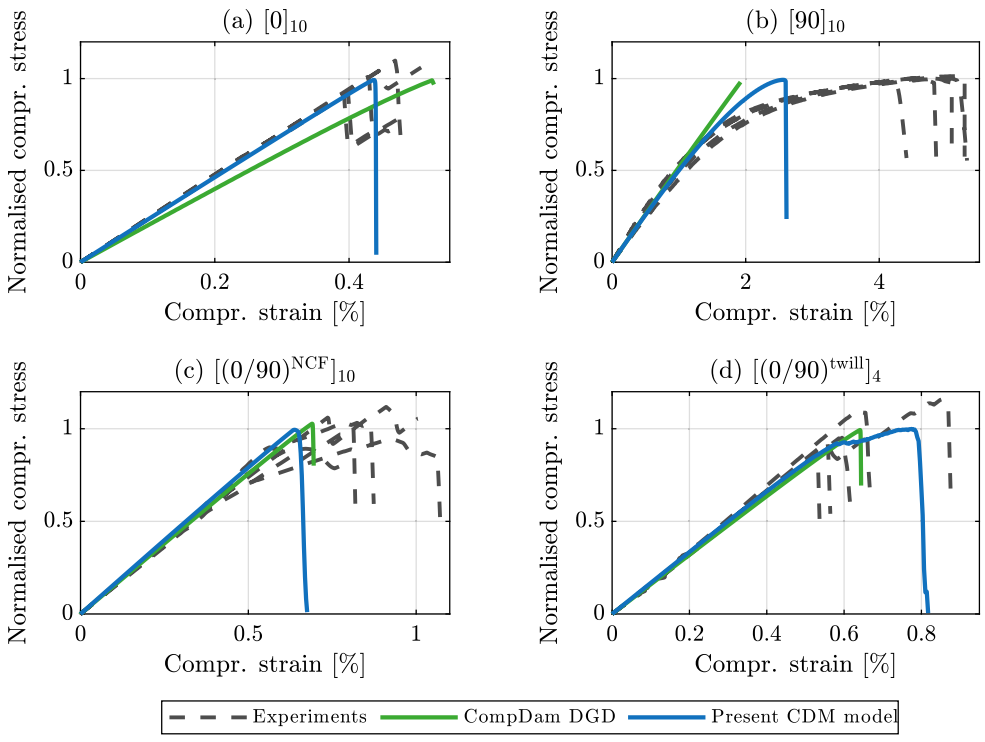

Fig. 15. Experimental and finite element simulation results of compression tests performed on UD, NCF and twill laminates. (a) Longitudinal compression test of UD laminate, (b) transverse compression test of UD laminate, (c)–(d) compression tests of NCF and twill laminates.

stress drop, the CDM model predicted significant stress hardening that exceeded the experimental peak load. For the model of Pinho et al. the first peak is the ultimate load. Considering laminate C — 45°, the predicted softening with the present CDM model is well aligned with experimental observations, while the model of Pinho et al. predicted a sharp drop in stress, and the NASA CompDam DGD code did not provide a converged solution in the softening region.

The experimentally measured compressive strengths of the laminates are compared with the predictions from the virtual simulations in Fig. 19. The predictions of the CDM model fall within the experimental range for most cases, with an average deviation of 6.14% from the experimental mean, while the measurements themselves show an average deviation of 3.80% from that mean. For comparison, the NASA CompDam code and the model of Pinho et al. resulted in average deviations of 8.07% and 8.75% from the experimental mean, respectively. It should be emphasised that parameter calibration has only been performed for the present CDM model and the NASA CompDam code, and recalibration of the initial misalignment angles for the model of Pinho et al. might influence the accuracy of the predictions for that model.

A similar comparison is conducted for the strains at the highest stress level shown in Fig. 20. A large scatter is observed in the experimental results, which suggests that more specimens per laminate type are needed to fairly account for statistical variations in the evaluation. It is hard to compare the performance of the different models regarding this measure due to the limited number of tests, but it can be concluded from Fig. 17 that the stress–strain curves predicted by the present CDM model qualitatively match the experimental ones in most cases.

5. Conclusions

A novel continuum damage mechanics-based material model has been proposed for the simulation of compressive failure of fibre-reinforced composite polymers. The model is based on mean-field homogenisation in the context of nonlinear kinematics. To achieve invariance to rigid-body rotations of the homogenised response consistently linked to a displacement fluctuation, a rotation-neutralised homogenisation is introduced. It appears that the resulting matrix–fibre continuity relations are expressed in terms of Biot stress. By assuming that the fibre phase is transversely isotropic hyperelastic and the matrix phase is isotropic hyperelastic, degraded by deviatoric continuum damage, a cost-effective CDM model is obtained for the failure analysis of UD composites under shear/compression. The model was also implemented in Abaqus/Explicit as a VUMAT subroutine.

Using the WWFE-III dataset, the mechanical response of an IM7/8552 UD composite was investigated in uniaxial and biaxial compression/shear stress states. This was done after calibrating the damage parameters to the transverse compressive curve and accounting for the initial misalignment in the longitudinal compressive strength. We emphasise that all response curves are developed solely on the calibrated damage parameters based on the uniaxial transverse compression test. For example, the damage model was validated based on the shear curve in Fig. 6, which showed good agreement between predicted and reported strength and strain at maximum stress. The biaxial failure curves generated with the proposed model showed similarities to the stress-based failure criteria for this dataset. Under combined longitudinal compression and shear, the close-to-linear LaRC05 failure envelope was obtained with high accuracy for large compressive stresses. Under combined transverse compression and shear, the failure envelope appears comparable to that of the Hashin model.

The model was also applied in compression tests of multidirectional laminates and was compared with two other well-established and relevant computational models from the literature. After the calibration of material parameters on simple laminates, the model predicted the compressive strength of six multidirectional laminates with an average deviation of 6.14% from the mean experimental value, which is lower than the NASA CompDam DGD code and the model of Pinho et al. whose average deviation from the mean experimental value was 8.07% and 8.75%, respectively. The post-peak response was qualitatively well-predicted with the CDM model in most cases. Brittle failure and a sharp stress drop are observed in the experiments, as well as in the model

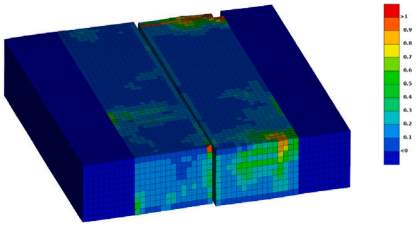

(a) $[0]_{10}$ Longitudinal compression

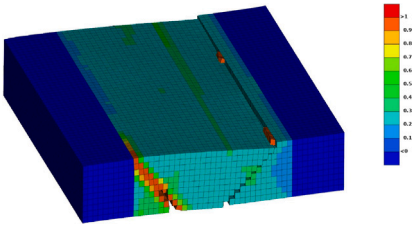

(b) $[90]_{10}$ Transverse compression

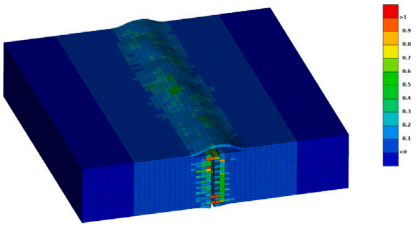

(c) $[(0/90)^{\mathrm{NCF}}]_{10}$ NCF compression

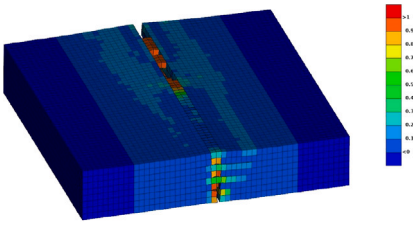

(d) $[(0/90)^{\mathrm{twill}}]_4$ Twill compression

Fig. 16. Based on the calibrated present CDM model, localised deformation patterns obtained from FE simulations of the laminates used for calibration. The images are coloured by the damage variable.

predictions for the laminates A — 0°, A — 45°, B — 0°, and C — 0°. A short softening region followed by a prolonged hardening region was predicted and experimentally observed for laminate B — 45°, and the rate of softening is also well-captured by the present model for laminate C — 45°.

A benefit of the isostatic/isostress conditions of the micromechanical response is that the effective longitudinal and transverse elastic stiffnesses are predicted with high accuracy. However, in-line with the isostress condition in shear, the initial longitudinal shear stiffness is underpredicted, with an accuracy level comparable to the inverse rule of mixtures. For the nonlinear part of the response, the consequence of the isostatic/isostress conditions is less apparent. As demonstrated in the laminate analyses, the initial weakening in shear does not play a significant role in the structural response due to the complex stress–strain states involved.

CRediT authorship contribution statement

Krisztián Gy. Hertelendy: Writing – original draft, Visualization, Validation, Software, Methodology, Formal analysis, Data curation. **Renaud Gutkin:** Writing – review & editing, Validation, Supervision, Methodology, Funding acquisition, Data curation. **Ragnar Larsson:** Writing – review & editing, Supervision, Funding acquisition, Formal analysis, Conceptualization.

Declaration of competing interest

The authors declare the following financial interests/personal relationships which may be considered as potential competing interests: Ragnar Larsson reports financial support was provided by Horizon Europe. If there are other authors, they declare that they have no known competing financial interests or personal relationships that could have appeared to influence the work reported in this paper.

Acknowledgement

The authors acknowledge funding from Horizon Europe through the MSCA Doctoral Network RELIANCE: REaL-tIme characterisation of ANisotropic Carbon-based tEchnological fibres, films, and composites, grant no. 101073040.

Appendix A. Modelling fibre-kinking failure in the model of pinho et al.

The stress state is first rotated to the fibre kinking plane defined by the axes $1 - 2^{\psi} - 3^{\psi}$ – the plane in which the fibres rotate — using the following transformations:

$$\sigma_{2^{\psi}2^{\psi}} = \frac{\sigma_{22}+\sigma_{33}}{2} + \frac{\sigma_{22}-\sigma_{33}}{2}\cos(2\psi) + \sigma_{23}\sin(2\psi), \tag{A.1}$$

$$\sigma_{3^{\psi}3^{\psi}} = \sigma_{22} + \sigma_{33} - \sigma_{2^{\psi}2^{\psi}}, \tag{A.2}$$

$$\sigma_{12^{\psi}} = \sigma_{12}\cos(\psi) + \sigma_{31}\sin(\psi), \tag{A.3}$$

$$\sigma_{2^{\psi}3^{\psi}} = -\frac{\sigma_{22}-\sigma_{33}}{2}\sin(2\psi) + \sigma_{23}\cos(2\psi), \tag{A.4}$$

$$\sigma_{3^{\psi}1} = \sigma_{31}\cos(\psi) - \sigma_{12}\sin(\psi). \tag{A.5}$$

Afterwards, the coordinate system is rotated around the axis 3^{ψ} in the kink-band, and the stress state is expressed in the misalignment frame defined by the axes $1^m - 2^m - 3^{\psi}$ as

$$\sigma_{1^m1^m} = \frac{\sigma_{11}+\sigma_{2^{\psi}2^{\psi}}}{2} + \frac{\sigma_{11}-\sigma_{2^{\psi}2^{\psi}}}{2}\cos(2\theta) + \sigma_{12^{\psi}}\sin(2\theta), \tag{A.6}$$

$$\sigma_{2^m2^m} = \sigma_{11} + \sigma_{2^{\psi}2^{\psi}} - \sigma_{1^m1^m}, \tag{A.7}$$

$$\sigma_{1^m2^m} = -\frac{\sigma_{11}-\sigma_{2^{\psi}2^{\psi}}}{2}\sin(2\theta) + \sigma_{12^{\psi}}\cos(2\theta), \tag{A.8}$$

$$\sigma_{2^m3^{\psi}} = \sigma_{2^{\psi}3^{\psi}}\cos(\theta) - \sigma_{3^{\psi}1}\sin(\theta), \tag{A.9}$$

$$\sigma_{3^{\psi}1^m} = \sigma_{3^{\psi}1^{\psi}}\cos(\theta). \tag{A.10}$$

The stress components in this coordinate system are used to calculate the normal and shear components of the traction vector at the fracture plane,

$$\sigma_n = \frac{\sigma_{2^m2^m}+\sigma_{3^m3^m}}{2} + \frac{\sigma_{2^m2^m}-\sigma_{3^m3^m}}{2}\cos(2\phi) + \sigma_{2^m3^{\psi}}\sin(2\phi), \tag{A.11}$$

$$\tau_T = -\frac{\sigma_{2^m2^m}-\sigma_{3^m3^m}}{2}\sin(2\phi) + \sigma_{2^m3^{\psi}}\cos(2\phi), \tag{A.12}$$

$$\tau_L = \sigma_{1^m2^m}\cos(\phi) + \sigma_{3^{\psi}1^m}\sin(\phi). \tag{A.13}$$

Finally, depending on the stress state, the matrix tension or compression criterion is applied to evaluate the failure index for fibre-kinking failure as

$$f_{\mathrm{kink}} = \begin{cases} \left(\frac{\tau_T}{S_T-\mu_T\sigma_n}\right)^2 + \left(\frac{\tau_L}{S_L-\mu_L\sigma_n}\right)^2, & \text{if} \quad \sigma_{2^m2^m} \le 0 \\ \left(\frac{\sigma_n}{Y_t}\right)^2 + \left(\frac{\tau_T}{S_T}\right)^2 + \left(\frac{\tau_L}{S_L}\right)^2, & \text{if} \quad \sigma_{2^m2^m} > 0. \end{cases} \tag{A.14}$$

For fibre-kinking failure, the constitutive response is linear elastic for $f_{\mathrm{kink}} < 1$. When f_{kink} reaches the value of 1, failure initiates, and the traction components presented in Eqs. (A.11)–(A.13) are linearly

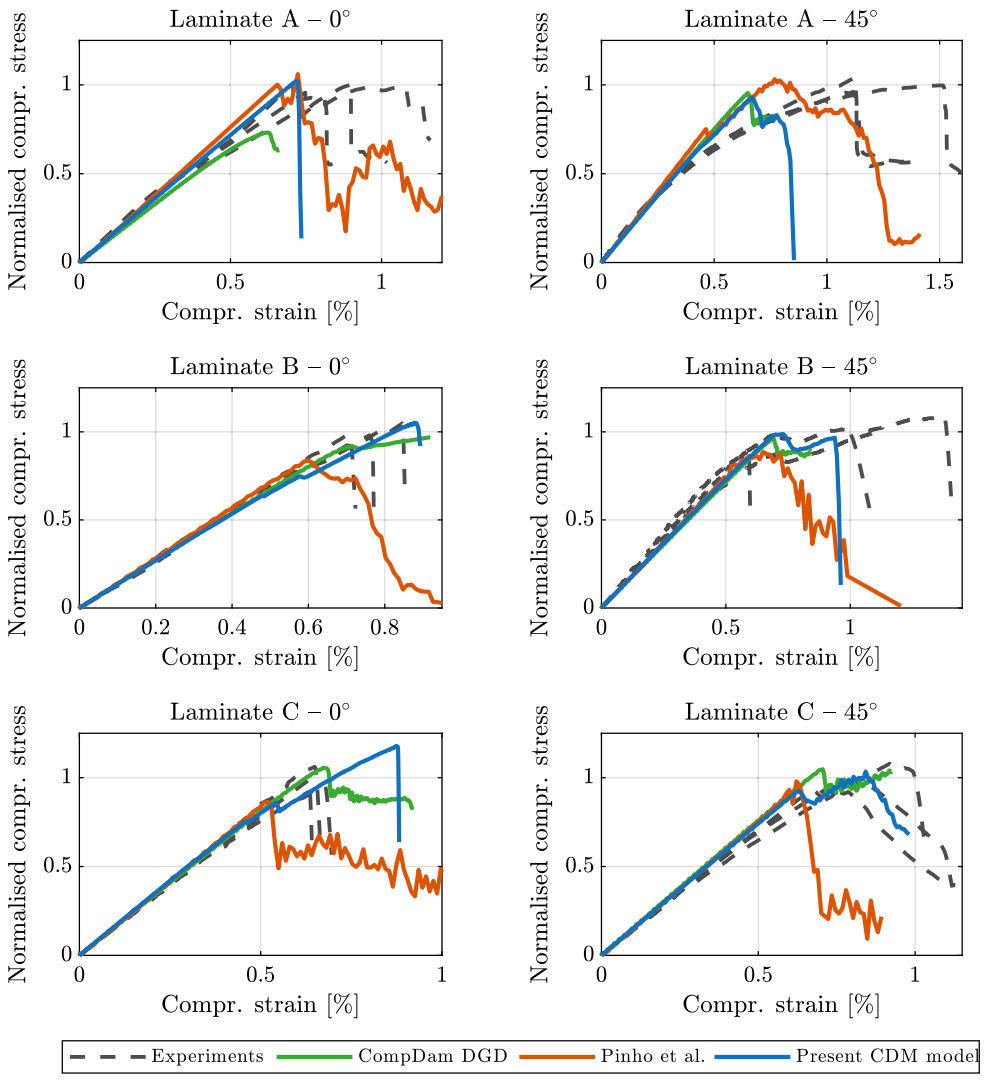

Fig. 17. Experimental and finite element simulation results of compression tests performed on Laminate A, B, and C in 0° and 45° orientations.

degraded. The softening slope is calculated on the basis of the energy dissipated by the finite element and is therefore scaled with the element length to achieve mesh independence.

Appendix B. Modelling fibre-kinking failure in the CompDam DGD model

If $\boldsymbol{F}$ denotes the average deformation gradient determined based on the nodal displacements of the finite element, $\boldsymbol{F}_{\mathrm{m}}$ denotes the deformation gradient in the undamaged part, $\boldsymbol{F}_{\mathrm{kb}}$ denotes the deformation gradient in the kinked part, and $\boldsymbol{F}^{(i)}$ denotes the ith column of the deformation gradient, then the relationships between the deformation gradients in the different regions are

$$\boldsymbol{F}_{\mathrm{kb}}^{(1)} = \frac{l_1}{w_{\mathrm{kb}}}\boldsymbol{F}^{(1)} + \left(1 - \frac{l_1}{w_{\mathrm{kb}}}\right)\boldsymbol{F}_{\mathrm{m}}^{(1)}, \tag{B.1}$$

$$\boldsymbol{F}_{\mathrm{kb}}^{(2)} = \boldsymbol{F}_{\mathrm{m}}^{(2)} = \boldsymbol{F}^{(2)}. \tag{B.2}$$

The initial fibre misalignment is denoted by φ_0 and can be either an in-plane or an out-of-plane misalignment. The two can be considered simultaneously, in which case the in-plane and out-of-plane rotations of the fibres are decoupled. Fig. 11(b) shows the case when the fibres are misaligned in-plane. The initial fibre direction is $\hat{\boldsymbol{E}}_f$, which can be expressed in the reference configuration as

$$\hat{\boldsymbol{E}}_f = \begin{bmatrix} \cos(\varphi_0) \\ \sin(\varphi_0) \\ 0 \end{bmatrix}. \tag{B.3}$$

The rotation of the fibres in the kinked region can be calculated by the deformation of the unit vector

$$\boldsymbol{e}_f = \boldsymbol{F}_{\mathrm{kb}} \cdot \hat{\boldsymbol{E}}_f, \tag{B.4}$$

from which the unit vector in the fibre direction in the current configuration can be obtained by normalisation as $\hat{\boldsymbol{e}}_f = \boldsymbol{e}_f/|\boldsymbol{e}_f|$. The current fibre rotation is then

$$\varphi = \tan^{-1}\left(\frac{R_{21}}{R_{11}}\right), \tag{B.5}$$

where

$$\boldsymbol{R} = \begin{bmatrix} \hat{\boldsymbol{e}}_f & \hat{\boldsymbol{e}}_n & \hat{\boldsymbol{e}}_t \end{bmatrix} \tag{B.6}$$

is the rotation matrix associated with the deformed configuration.

The actual rotation is determined based on traction continuity on a plane defined by the rotated fibre direction as

$$\boldsymbol{\sigma}_{\mathrm{kb}} \cdot \hat{\mathbf{e}}_f = \boldsymbol{\sigma}_{\mathrm{m}} \cdot \hat{\mathbf{e}}_f. \tag{B.7}$$

The model also considers shear nonlinearity in the misaligned frame with a one-dimensional plastic model. In the current application, the

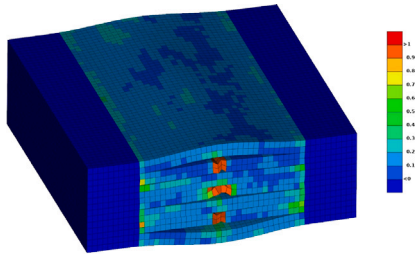

(a) Laminate A – 0°

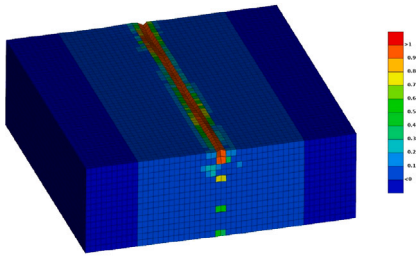

(b) Laminate A – 45°

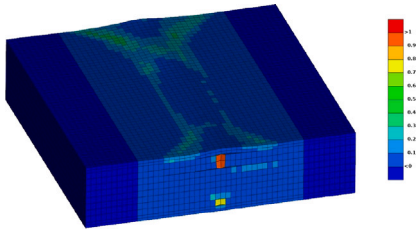

(c) Laminate B – 0°

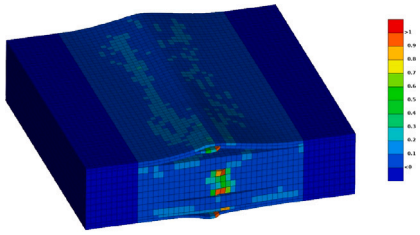

(d) Laminate B – 45°

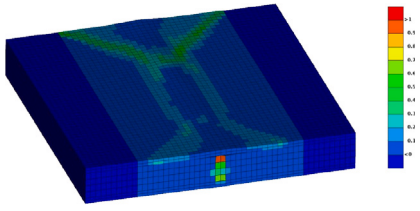

(e) Laminate C – 0°

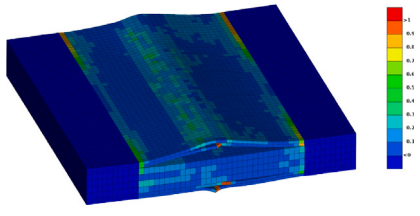

(f) Laminate C – 45°

Fig. 18. Deformation patterns of Laminates A, B and C in the validation simulations using the present CDM model. The images are coloured by the damage variable.

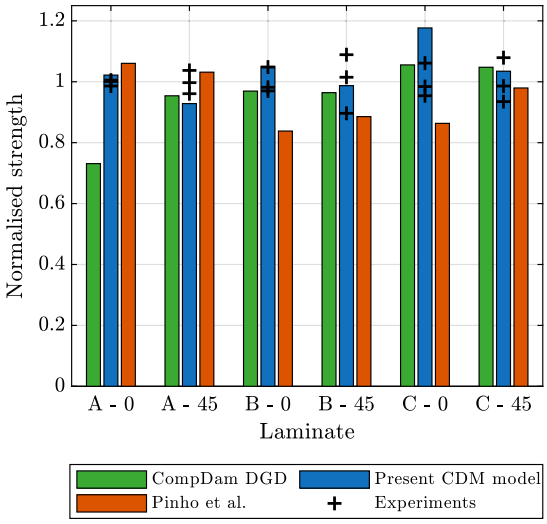

Fig. 19. Experimental and predicted compressive strengths by the model for the different laminates.

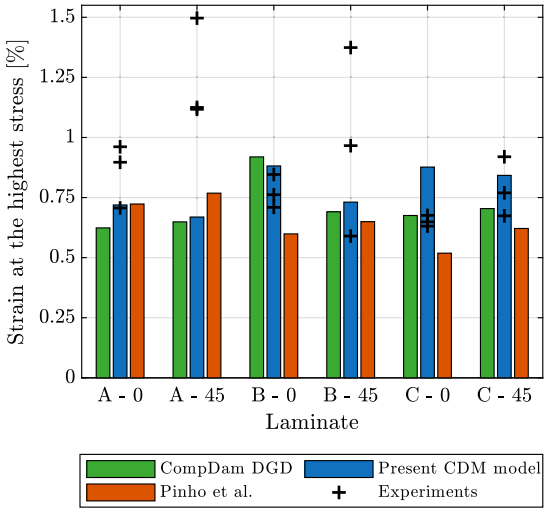

Fig. 20. Strain at the highest stress — experimental and predicted by the model for the different laminates.

Ramberg–Osgood expression is used to model shear nonlinearity, expressed as

$$\gamma_{12} = \frac{1}{G_{12}} \left(\tau_{12} + \text{sign}(\tau_{12})\, \alpha\, |\tau_{12}|^n \right) \tag{B.8}$$

for in-plane rotation of the fibres, where γ_{12} is the shear strain, G_{12} the elastic shear modulus, τ_{12} the shear stress, and α and n are parameters describing the nonlinear strain hardening behaviour. It is also possible to include elastic nonlinearity in the fibre direction, in which case the longitudinal Young's modulus is linearly dependent on the longitudinal normal strain as

$$E_1^* = E_1(1 + c^l \varepsilon_{11}), \tag{B.9}$$

where E_1^* is the tangential longitudinal Young's modulus, E_1 the initial longitudinal Young's modulus, and c^l a nonlinearity coefficient.

Data availability

The authors do not have permission to share data.

References

Affdl, J.C.H., Kardos, J.L., 1976. The Halpin-Tsai equations: A review. Polym. Eng. Sci. 16 (5), 344–352.

Andersson, A., Ståhl, K., 2019. Virtual durability testing of CFRP materials. URL https://hdl.handle.net/20.500.12380/256757.

Argon, A.S., 1972. Fracture of composites. In: Herman, H. (Ed.), In: Treatise on Materials Science & Technology, vol. 1, Elsevier, pp. 79–114.

Bai, Y., Zhao, Z., Duan, S., Wang, P., Li, Y., Lei, H., 2025. Internal shear damage evolution of CFRP laminates ranging from -100° c to 100° c using in-situ X-ray computed tomography. Compos. Sci. Technol. 259.

Bergan, A.C., Herráez, M., González, C., Lopes, C.S., 2020. A constitutive model for fiber kinking: Formulation, finite element implementation, and verification. Compos. Part A: Appl. Sci. Manuf. 129.

Bergan, A., Jackson, W., 2018. Validation of a Mesoscale Fiber Kinking Model through Test and Analysis of Double Edge Notch Compression Specimens. Am. Soc. Compos. 2022.

Budiansky, B., 1983. Micromechanics. Comput. Struct. 16 (1), 3–12.

Budiansky, B., Fleck, N.A., 1993. Compressive failure of fibre composites. J. Mech. Phys. Solids 41 (1), 183–211.

Dassault Systèmes, 2024. Defining the Constitutive Response of Cohesive Elements Using a Traction-Separation Description. SIMULIA, URL https://help.3ds.com/2024/English/DSSIMULIA_Established/SIMACAEELMRefMap/simaelm-c-cohesivebehavior.htm.

Dávila, C.G., Camanho, P.P., 2003. Failure Criteria for FRP Laminates in Plane Stress. Tech. Rep. NASA/TM-2003-212663, National Aeronautics and Space Administration, U.S.A..

Eshelby, J.D., 1957. The determination of the elastic field of an ellipsoidal inclusion, and related problems. Proc. Soc. Lond. Ser. A. Math. Phys. Sci. 241 (1226), 376–396.

Fallahi, H., Taheri-Behrooz, F., Asadi, A., 2019. Nonlinear mechanical response of polymer matrix composites: A review. Polym. Rev. 60, 1–44.

Fleck, N.A., Sivashanker, S., Sutcliffe, M.P.F., 1997. Compressive failure of composites due to microbuckle growth. Eur. J. Mech. A Solids 16, 65–82, Special issue on micromechanics of materials.

Hashin, Z., 1980. Failure criteria for unidirectional fiber composites. J. Appl. Mech. 47 (2), 329–334.

Herraez, M., Bergan, A.C., Gonzalez, C., Lopes, C.S., 2018. Modeling fiber kinking at the microscale and mesoscale. NASA Tech. Rep. Serv. (NASA) URL https://ntrs.nasa.gov/api/citations/20180007919/downloads/20180007919.pdf.

Hinton, M.J., 2004. Failure Criteria in Fibre-Reinforced-Polymer Composites: The World-Wide Failure Exercise. Elsevier, URL http://ci.nii.ac.jp/ncid/BA69724894.

Hinton, M.J., Kaddour, A.S., 2012. The background to the second world-wide failure exercise. J. Compos. Mater. 46 (19–20), 2283–2294.

Kabiri Ataabadi, A., Hosseini-Toudeshky, H., Ziaei Rad, S., 2014. Experimental and analytical study on fiber-kinking failure mode of laminated composites. Compos. Part B: Eng. 61, 84–93.

Kaddour, A.S., Hinton, M.J., Smith, P.A., Li, S., 2013a. The background to the third world-wide failure exercise. J. Compos. Mater. 47 (20–21), 2417–2426.

Kaddour, A.S., Hinton, M.J., Smith, P.A., Li, S., 2013b. Mechanical properties and details of composite laminates for the test cases used in the third world-wide failure exercise. J. Compos. Mater. 47 (20–21), 2427–2442.

Khatam, H., Pindera, M.-J., 2009. Parametric finite-volume micromechanics of periodic materials with elastoplastic phases. Int. J. Plast. 25.

Larsson, R., Brambati, G., Gutkin, R., 2023. Compressive failure and kink-band formation modeling. Eur. J. Mech. A Solids 99.

Larsson, R., Gutkin, R., Rouhi, M.S., 2018. Damage growth and strain localization in compressive loaded fiber reinforced composites. Mech. Mater. 127, 77–90.

Larsson, F., Runesson, K., Su, F., 2010. Variationally consistent computational homogenization of transient heat flow. Internat. J. Numer. Methods Engrg. 81.

Leone, F.A., 2015. Deformation gradient tensor decomposition for representing matrix cracks in fiber-reinforced materials. Compos. Part A: Appl. Sci. Manuf. 76, 334–341.

Leone, F.A., Bergan, A.C., Dávila, C.G., 2019. CompDam - Deformation gradient decomposition (DGD), v2.5.0. https://github.com/nasa/CompDam_DGD.

Ma, L., Liu, F., Liu, D., Liu, Y., 2021. Review of strain rate effects of fiber-reinforced polymer composites. Polymers 13 (17).

Mandal, T., Nguyen, V.P., Wu, J.-Y., 2019. Length scale and mesh bias sensitivity of phase-field models for brittle and cohesive fracture. Eng. Fract. Mech. 217.

Melin, L.G., Neumeister, J.M., Pettersson, K.B., Johansson, H., Asp, L., 2000. Evaluation of four composite shear test methods by digital speckle strain mapping and fractographic analysis. J. Compos. Technol. Res. 22, 161–172.

Pinho, S., Darvizeh, R., Robinson, P., Schuecker, C., 2012. Material and structural response of polymer-matrix fibre-reinforced composites. J. Compos. Mater. 46, 2313–2341.

Pinho, S.T., Iannucci, L., Robinson, P., 2006a. Physically-based failure models and criteria for laminated fibre-reinforced composites with emphasis on fibre kinking: Part I: Development. Compos. Part A: Appl. Sci. Manuf. 37 (1), 63–73.

Pinho, S.T., Iannucci, L., Robinson, P., 2006b. Physically based failure models and criteria for laminated fibre-reinforced composites with emphasis on fibre kinking. Part II: FE implementation. Compos. Part A: Appl. Sci. Manuf. 37 (5), 766–777.

Pinho, S.T., Robinson, P., Iannucci, L., 2006c. Fracture toughness of the tensile and compressive fibre failure modes in laminated composites. Compos. Sci. Technol. 66 (13), 2069–2079.

Singh, V., Larsson, R., Olsson, R., Marklund, E., 2024. Rate dependent compressive failure and delamination growth in multidirectional composite laminates. J. Compos. Mater. 58 (3), 419–431.

Truong, T.C., Vettori, M., Lomov, S., Verpoest, I., 2005. Carbon composites based on multi-axial multi-ply stitched preforms. Part 4. Mechanical properties of composites and damage observation. Compos. Part A: Appl. Sci. Manuf. 36 (9), 1207–1221.

Wang, J., Xiao, Y., Kawai, M., Inoue, K., 2018. Observation and modeling of loading–unloading hysteresis behavior of unidirectional composites in compression. J. Reinf. Plast. Compos. 37 (5), 287–299.

Wilhelmsson, D., Fredrik, E., Gutkin, R., Asp, L., 2020. The transition from out-of-plane to in-plane kinking due to off-axis loading. Chalmers Res. (Chalmers Univ. Technology) URL https://research.chalmers.se/en/publication/503863.